

Aircraft-derived particle fluxes distinguish entrainment zone and decoupled layer nucleation in marine boundary layers

Ajmal Rasheeda Satheesh¹, Markus D. Petters², and Nicholas Meskhidze¹

¹Department of Marine, Earth, and Atmospheric Sciences, North Carolina State University, Raleigh, NC 27695, USA.

²Department of Chemical and Environmental Engineering, University of California, Riverside, CA 92521, USA.

Corresponding author: Nicholas Meskhidze (nmeskhidze@ncsu.edu)

Abstract

3–10 nm sized particles, defined as "small particle event" (SPE), play a critical role in marine boundary layer aerosol budgets and aerosol–cloud interactions, yet the vertical distribution of their sources remains poorly constrained. We identified the vertical location of SPEs by deriving turbulent fluxes of 3–10 nm particles from aircraft measurements during the Aerosol and Cloud Experiments in the Eastern North Atlantic (ACE-ENA) campaign. To overcome stationarity limitations of traditional eddy covariance methods, we applied continuous wavelet transform analysis to data collected during June–July 2017 and January–February 2018 flights over the Azores. Our flux-based analysis revealed two distinct SPE scenarios with different vertical structures and spatial extents. The first featured nucleation in the entrainment zone, where free tropospheric air entrains into the boundary layer. The second showed nucleation in the decoupled layer, a stratified region between the well-mixed surface layer and cloud-topped upper boundary layer. In both cases, convergence of air masses from different layers diluted preexisting aerosol surface area to very low levels, creating conditions favorable for nucleation and generating strong downward particle fluxes. SPEs occurred in 15% of flights, challenging prevailing theoretical expectations that new particle formation should rarely occur in marine boundary layers due to high condensation and coagulation sink capacity of sea spray aerosols. Aircraft-derived particle fluxes provide first observational constraints on the vertical location and source strength of likely nucleation regions in the remote marine boundary layer, improving aerosol source representations in climate models and reducing uncertainties in aerosol–cloud interactions.

1. Introduction

Cloud adjustments due to aerosols constitute one of the most significant uncertainties in climate modeling (Intergovernmental Panel on Climate Change (IPCC), 2023). The magnitude of anthropogenic aerosol radiative forcing over the industrial period is strongly influenced by the abundance and properties of natural aerosols (Andreae, 2007; Carslaw et al., 2013; Hoose et al., 2009; Meskhidze et al., 2011). While uncertainties in aerosol radiative forcing from different processes (emissions, long-range transport, new particle formation, and removal) vary spatially, marine boundary layer (MBL) cloud microphysical properties exhibit the highest sensitivity to aerosol changes (Bellouin et al., 2020; Zhang et al., 2024). Understanding how marine low level clouds and their radiative effects respond to changing aerosol load is important due to their extensive spatial coverage, low optical thickness, and low background cloud condensation nuclei (CCN) concentrations. The response of these clouds to changes in aerosol loading remains

Formatted: Font color: Blue

Formatted: Font: Not Bold

Formatted: Font: Not Bold

Formatted: Font: Not Bold

Formatted: Font: Not Bold

Formatted: Font: Not Bold

Formatted: Font: Not Bold

Formatted: Font: Not Bold

Formatted: Font: Not Bold

Formatted: Font: Not Bold

Formatted: Font: Not Bold

Formatted: Font: Not Bold

Formatted: Font: Not Bold

Formatted: Font: Not Bold

Formatted: Font: Not Bold

Formatted: Font: Not Bold

Formatted: Font: Not Bold

Formatted: Font: Not Bold

Formatted: Font: Not Bold

Formatted: Font: Not Bold

Formatted: Font: Not Bold

Formatted: Font: Not Bold

Formatted: Font: Not Bold

Formatted: Font: Not Bold

Formatted: Font: Not Bold

Formatted: Font: Not Bold

Formatted: Font: Not Bold

Formatted: Font: Not Bold

Formatted: Font: Not Bold

Formatted: Font: Not Bold

Formatted: Font: Not Bold

Formatted: Font: Not Bold

Formatted: Font: Not Bold

Formatted: Font: Not Bold

Formatted: Font: Not Bold

Formatted: Font: Not Bold

Formatted: Font: Not Bold

Formatted: Font: Not Bold

Formatted: Font: Not Bold

Formatted: Font: Not Bold

Formatted: Font: Not Bold

Formatted: Font: Not Bold

Formatted: Font: Not Bold

Formatted: Font: Not Bold

Deleted: Abstract New particle formation (NPF) in marine boundary layers plays a critical role in cloud condensation nuclei (CCN) budgets and aerosol–cloud interactions, yet the vertical distribution of NPF sources, critical for predicting CCN production efficiency, remains poorly constrained. We identified the vertical location of NPF events by deriving turbulent fluxes of 3–10 nm particles from aircraft measurements during the Aerosol and Cloud Experiments in the Eastern North Atlantic (ACE-ENA) campaign. To overcome stationarity limitations of traditional eddy covariance methods, we applied continuous wavelet transform analysis to data collected during June–July 2017 and January–February 2018 flights over the Azores. Our flux-based analysis revealed two distinct NPF scenarios with fundamentally different vertical structures and spatial extents. The first scenario featured nucleation in the entrainment zone, where free tropospheric air entrains into the boundary layer. The second scenario showed nucleation in the decoupled layer, a stratified region between the well-mixed surface layer and cloud-topped upper boundary layer. Both cases exhibited strong downward particle fluxes driven by similar mechanisms: air masses meeting from different layers and mixing, which diluted aerosols to very low total particle surface area, creating favorable nucleation conditions. NPF occurred in 15% of flights, challenging prevailing theoretical expectations that NPF should rarely occur in marine boundary layers due to high condensation and coagulation sinks from sea spray aerosols. Aircraft-derived aerosol fluxes provide essential observational constraints on the vertical distribution and source strength of new particle formation in marine environments, enabling improved representation of these processes in climate models.⁴

62 poorly constrained and represents a key source of uncertainty in climate projections (Zhang et al., 2024).
63 Consequently, understanding aerosol composition, dynamics, and the mechanisms controlling CCN number budgets
64 within the MBL is critical for improving climate models and reducing predictive uncertainties. While freshly nucleated
65 particles in the 3–10 nm size range must undergo substantial growth before reaching CCN-relevant sizes (>50–80
66 nm), this growth pathway is well established in marine environments. At typical marine boundary layer growth rates
67 of 1–3 nm hr⁻¹ (Ehn et al., 2010; Nieminen et al., 2018; O’Dowd et al., 2010; Zheng et al., 2018), newly formed
68 particles can reach CCN sizes within 24–48 hours. This timescale is consistent with air mass residence times in the
69 remote marine boundary layer (Kulmala et al., 2012; Zheng et al., 2021). Constraining the vertical location and flux
70 magnitude of freshly nucleated particles therefore represents a critical first step toward understanding the full aerosol
71 number budget in marine environments, including the ultimate contribution of NPF to CCN populations.

Formatted: Font color: Blue

72 Previous studies have identified three primary aerosol sources in remote MBLs: (1) long-range continental transport
73 (Logan et al., 2014), (2) downward mixing of particles formed in the free troposphere (FT) through new particle
74 formation (NPF) mechanisms (Clarke et al., 2013), and (3) sea spray emissions (Quinn et al., 2017). NPF occurring
75 either near the top of stratocumulus cloud decks within open-cell regions (Petters et al., 2006) or in the upper portions
76 of mid-latitude MBLs (Zheng et al., 2021) has been suggested as an important in-situ aerosol source within the MBL.
77 However, the difficulty in capturing actual nucleation events and determining their precise vertical location has led to
78 the prevailing theoretical view that NPF should rarely occur in remote marine boundary layers over open oceans. This
79 expectation is based on the high condensation and coagulation sink capacity of the remote MBL, which includes not
80 only sea spray aerosols (Bates et al., 1998; Pirjola et al., 2000) but also accumulation-mode sulfate and organic
81 particles entrained from the free troposphere (Yoon et al., 2001). Clouds further suppress NPF by scavenging Aitken-
82 mode particles (Zheng et al., 2018), accelerating sulfate production on existing droplets through aqueous-phase SO₂
83 oxidation (Sanchez et al., 2021), and sequestering DMS oxidation products such as Hydroperoxymethyl thioformate
84 (HPMTF) that would otherwise contribute to sulfuric acid formation (Novak et al., 2021). Independent corroboration
85 of in-situ NPF over the eastern North Atlantic comes from the Azores Stratocumulus Measurements of Radiation,
86 Turbulence and Aerosols (ACORES) campaign, which conducted helicopter-borne observations over Graciosa Island
87 in July 2017, overlapping in time and location with the ACE-ENA campaign analyzed here. Siebert et al., (2021)
88 reported frequent burst-like freshly nucleated particle events near the stratocumulus cloud top and in the free
89 troposphere, while also noting that these particles did not grow to CCN-relevant sizes within the ~2-hour observation
90 window. This outcome is expected given the 24–48 hour growth timescales discussed above. These concentration-
91 based observations, however, could not determine the precise vertical location of the nucleation source regions,
92 motivating the flux-based approach developed in the present study.

Moved (insertion) [1]

Moved up [1]: (Bates et al., 1998; Pirjola et al., 2000).

Deleted: This expectation is based on the relatively high surface area of sea spray aerosols, which act as condensation and coagulation sinks for nucleating vapors and newly formed particles

Deleted:

Formatted: Font color: Blue

Deleted: ¶

93 Determining the vertical origin of freshly nucleated particles, whether from the free troposphere, the interfacial layer
94 near the marine boundary layer–free troposphere boundary, or the interface between the well-mixed marine boundary
95 layer and decoupled layer, has critical implications for both fundamental understanding and climate modeling.
96 Knowledge of where nucleation occurs is essential for understanding aerosol formation mechanisms and enabling
97 climate models to accurately simulate aerosol number size distributions required for radiative calculations. Most
98 atmospheric models have historically assumed that nucleation should be negligible in marine boundary layers, instead

105 predicting that particle formation would be favored at high altitudes where both temperature and aerosol surface area
106 are substantially lower. However, traditional time-averaged aerosol concentration measurements from aircraft
107 campaigns provide limited information about the precise vertical location where nucleation events occur. This
108 limitation has prevented definitive identification of nucleation zones within the marine boundary layer and hampered
109 efforts to constrain the relative importance of different aerosol sources to marine aerosol budgets. Without direct
110 observational evidence of where particles form, climate models continue to rely on theoretical assumptions that may
111 not accurately represent actual nucleation processes in marine environments.

112 To address this critical knowledge gap, vertical turbulent flux measurements of freshly nucleated 3–10 nm particles
113 have emerged as particularly valuable tools for inferring the vertical location of likely nucleation source regions (Islam
114 et al., 2022). The flux direction provides indirect evidence of the likely nucleation location; positive (upward) fluxes
115 indicate nucleation below the aircraft, while negative (downward) fluxes suggest nucleation above the aircraft. This
116 approach offers unprecedented spatial and temporal resolution for identifying nucleation zones that cannot be detected
117 through conventional concentration measurements alone. In this study, we derive vertical turbulent fluxes of 3–10 nm
118 particles using data collected during the Aerosol and Cloud Experiments in the Eastern North Atlantic (ACE-ENA)
119 campaign. The campaign comprised two intensive operational periods (IOPs) – summer 2017 and winter 2018 –
120 utilizing the G1 research aircraft from the DOE Atmospheric Radiation Measurement (ARM) program. By applying
121 continuous wavelet transform techniques to high-frequency aircraft measurements, we provide the first flux-based
122 observational constraints on the vertical distribution of likely NPF source regions in remote marine boundary layers,
123 enabling improved representation of aerosol sources in climate models.

124 2. Materials and Methods

125 2.1 Sampling Site

126 The Department of Energy Atmospheric Radiation Measurement (DOE–ARM) Eastern North Atlantic (ENA) facility
127 is positioned on Graciosa Island within the Azores archipelago, located in the northeastern Atlantic Ocean to the west
128 of Portugal (Mather and Voyles, 2013). Air mass transport to this location follows four main pathways: (1) polluted
129 outflow from North American sources, (2) continental emissions originating from northern European regions, (3)
130 relatively clean Arctic air masses, and (4) air masses that recirculate within the Azores High pressure system (Wood
131 et al., 2015; Zheng et al., 2018). The location is characterized by a low average annual aerosol optical depth (AOD)
132 of 0.12 (Logan et al., 2014).

133 Data collection for this research occurred during the ACE-ENA field campaign, which included two intensive
134 observation periods (IOPs): the initial period ran from June 21 to July 20, 2017, while the second period extended
135 from January 15 to February 18, 2018 (Wang et al., 2019). All data from the ARM ENA site are publicly accessible
136 through the ARM Data Discovery tool.

Deleted: CCN

Formatted: Font color: Blue

Deleted: vertical turbulent flux measurements of freshly nucleated particles have emerged as particularly valuable tools for characterizing the vertical location of particle nucleation

Deleted: The flux direction provides direct evidence of nucleation location...

Deleted: we provide the first direct observational constraints on the vertical distribution of new particle formation

145 **2.2 Instrumentation**

146 This study utilized datasets from the ARM Aerial Facility (Schmid et al., 2014). The G-1 research aircraft was
147 equipped with over 50 instruments for comprehensive measurements of aerosols, clouds, and atmospheric processes.
148 Detailed information regarding flight patterns executed during the campaign can be found in (Wang et al., 2019).
149 Two Condensation Particle Counters (CPCs, models 3025A and 3772, TSI Inc.) with nominal 50% counting efficiency
150 cutoff diameters of 3 nm and 10 nm, respectively, sampled through an isokinetic inlet exhibiting >90% efficiency for
151 particles with aerodynamic diameters below 5 μm . The concentration of 3–10 nm sized particles was calculated as the
152 difference between these CPC measurements and is denoted as N_{3-10} throughout this paper. Since the measurements
153 did not extend to particle sizes small enough to directly identify nucleation events, we follow (Islam et al., 2022) in
154 using the term "small particle event" (SPE) to characterize these observations. The CPC 3772 operated at a constant
155 1 LPM flow rate maintained by an external pump and critical orifice (Fan and Pekour, 2018), while the CPC 3025A
156 sample flow rate was not actively controlled. Both flow rates remained stable across the sampling altitude range
157 (Zheng et al., 2021). The airborne CPC configuration was validated for operation up to 4000 m altitude and across
158 ambient relative humidity conditions of 0–90% RH. For a typical polluted environment ($\sim 5000 \text{ cm}^{-3}$), CPC
159 concentration measurements had an accuracy of 0.3 % (Kuang and Mei, 2019). All data used in this study passed
160 instrument mentor specified quality control filters, which are distributed alongside the data.

161 Vertical wind speed (w) was measured using the Aircraft Integrated Meteorological Measurement System probe
162 (AIMMS-20, Aventech Research Inc.). The raw measurements define downward movement as positive; therefore,
163 the sign was inverted to align with meteorological convention (positive values indicating updrafts and negative values
164 indicating downdrafts). Although measurements were recorded at 20 Hz, they were downsampled to 1 Hz to match
165 the temporal resolution of the CPC data acquisition.

166 Aerosol size distributions from 10 nm to 600 nm were characterized using a Fast Integrated Mobility Spectrometer
167 (FIMS) (Kulkarni and Wang, 2006a, b). The FIMS provides size distribution measurements at 1-second temporal
168 resolution with signal-to-noise characteristics suitable for detecting both remote continental and clean marine aerosol
169 concentrations, as demonstrated in aircraft-based deployments (Kulkarni and Wang, 2006a, b; Olfert et al., 2008).

170 Particles are charged within the instrument and separated by electrical mobility using an applied electric field. The
171 separated particles are subsequently grown into supermicron droplets in a condenser and imaged with a high-speed
172 camera. This approach enables the FIMS to deliver size distribution measurements comparable to those of Scanning
173 Mobility Particle Sizers (SMPS), but at a significantly higher time resolution. This study employed an advanced FIMS
174 configuration utilizing a spatially varying electric field that extends the measurement range from 10 nm to 600 nm
175 (Wang et al., 2017b, a). Size distribution measurements were normalized to dry conditions; therefore, reported size
176 distributions and number concentrations do not represent ambient humidity conditions. Cloud contamination filters
177 were applied to prevent misclassification of cloud droplets as aerosol particles, with detailed filtering procedures
178 described in the following section. FIMS-derived number concentration also served as a quality control flag for the
179 CPC 3772. Since both instruments share an overlapping detection size range (10–600 nm for FIMS; >10 nm for CPC
180 3772), their total number concentrations should be broadly comparable under normal operating conditions. CPC
181 concentrations falling below 10% of the simultaneously measured FIMS concentration indicate a physically

Deleted: -

Deleted: 1

Deleted: The FIMS provides high temporal resolution measurements with excellent sensitivity and counting statistics required for aircraft-based studies (Olfert et al., 2008)

187 implausible discrepancy inconsistent with real atmospheric variability and were therefore excluded from analysis as
188 likely instrument malfunctions.
189 A two-dimensional stereo probe (2D-S) was used to retrieve drizzle concentration. It uses shadowgraphy to measure
190 size distribution of hydrometeor particles in the size range 15 μm to 2.5 mm (Glienke and Mei, 2019). All data
191 products are publicly available through the ARM DOE website with citations in the data availability section and have
192 undergone quality control by instrument mentors. Additional technical details are available in the corresponding
193 citations.

194 2.3 Data Reduction

195 2.3.1 Droplet shattering and cloud contamination

196 Droplet shattering represents a significant source of measurement contamination in airborne aerosol sampling studies.
197 Weber et al., (1998) described this phenomenon as the fragmentation of cloud droplets during in-cloud measurements,
198 which can produce artifacts as small as 3 nm that appear in sampling instruments. Similarly, Korolev and Isaac, (2005)
199 documented comparable shattering effects with ice particles. While a detailed examination of the physical mechanisms
200 behind droplet shattering lies beyond this study's scope, it is essential to filter such artifacts from our dataset to prevent
201 misidentification of SPEs.

202 Cloud contamination was systematically detected and eliminated by calculating liquid water content (LWC) using the
203 approach of Zheng et al., (2021), which utilizes droplet size spectra from the Fast Cloud Droplet Probe (FCDP). Visual
204 data examination established a detection threshold of $3 \times 10^{-3} \text{ g m}^{-3}$, comparable to the 10^{-3} g m^{-3} threshold employed
205 by Zheng et al., (2021). Data exceeding this LWC threshold were excluded from analysis.

206 2.3.2 Time lag correction

207 Accurate temporal alignment between the vertical wind speed measured by the AIMMS-20 probe and the particle
208 concentration measured by the CPCs is essential for reliable flux calculations. Because these instruments were located
209 at different positions on the aircraft, a time lag exists between the two signals that must be determined and corrected
210 prior to flux calculation.

211 To confirm that the two CPCs sampled identical air masses simultaneously, Spearman correlation coefficients were
212 calculated for concentration measurements from both CPCs after removing cloud shattering artifacts and excluding
213 SPE periods. From the complete campaign dataset, 370 randomly selected seconds of data yielded an average
214 Spearman correlation coefficient of 0.97 (Supplementary Figs. S1–S2), confirming adequate synchronization between
215 the two concentration records. However, a high correlation coefficient alone does not determine the precise temporal
216 offset between the two signals.

217 Lag times between the two CPC signals were determined individually for every 20-second interval (representing the
218 time taken for the airplane to traverse 2 km) using covariance maximization, shifting one CPC relative to the other
219 signal to identify the temporal offset that maximizes their covariance. A single fixed lag time across the entire
220 campaign was not appropriate, given the variability in lag times observed across flight segments (Supplementary Fig.

Deleted: FIMS-derived number concentration also served as a quality control flag for the 3772 CPC, where CPC concentrations less than 10% of corresponding FIMS concentrations were excluded from analysis.

Deleted: A single-particle soot photometer (SP2) measured refractory black carbon concentrations in the 50 nm – 500 nm size range. While the SP2 detects individual particles and can provide number concentrations, this study reports mass concentrations (ng m^{-3}) (Schwarz et al., 2006). A high-resolution time-of-flight aerosol mass spectrometer (HR-ToF-AMS) measured bulk nonrefractory aerosol composition including sulfate, nitrate, ammonium, and organics. Dimethylsulfide (DMS) concentrations were measured using a quadruple high-sensitivity Proton-Transfer-Reaction Time-of-Flight Mass Spectrometer (PTR-ToF-MS). Due to measurement uncertainties (Zheng et al., 2021) DMS data indicate presence along the flight track rather than providing precise quantification.

S3). This approach was independently validated using pressure measurements from the isokinetic inlet and static pressure from the AIMMS-20 probe. The two pressure records yielded a Spearman correlation coefficient of 0.99, confirming that both instruments consistently sampled the same air mass with no systematic offset (Supplementary Fig. S5). Similarly, covariance maximization applied to the pressure records confirmed that no single lag time was appropriate across the full campaign (Supplementary Fig. S6), consistent with the CPC-based analysis and further supporting the use of individually determined lag times for each flux calculation period.

2.4 Aerosol number flux calculations

Flux measurement methods were originally developed for tower-based platforms, and their application to aircraft measurements introduces fundamental differences in sampling characteristics that must be carefully considered. Tower measurements provide continuous observations at fixed heights, capturing the complete turbulent eddy spectrum including low-frequency contributions essential for accurate flux estimates (Helbig et al., 2021; Sakai et al., 2001). Aircraft measurements, by contrast, sample different air masses as the platform moves horizontally, effectively trading temporal for spatial averaging (Desjardins et al., 1989)

Three interconnected challenges arise specifically for aircraft-based flux measurements. First, turbulent intensity in convective boundary layers increases with height above the surface layer before decreasing above $0.3\text{--}0.4 z_i$ (where z_i is the boundary layer height). Maintaining flux variance within 10% therefore requires measurement lengths of 100 to 10^4 times the boundary layer height (Lenschow and Stankov, 1986), a constraint that becomes increasingly difficult to satisfy at the higher altitudes routinely sampled by research aircraft. Second, high aircraft speeds impose strict constraints on sensor response times: for an aircraft traveling at 100 m s^{-1} , a 1 Hz sampling system resolves eddies no smaller than 200 m, approaching the lower limit for capturing the dominant flux-carrying scales. The CPCs used in this study operate at 1 Hz, meaning that contributions from smaller eddies are not resolved and must be accounted for through flux loss corrections (Section 2.8). Third, and most critically for flux calculation, aircraft measurements are inherently non-stationary as the platform continuously moves through different air masses, meteorological conditions, and altitudes. Traditional eddy covariance methods assume stationarity over the averaging period, a condition that is difficult to maintain during aircraft sampling (Gioli et al., 2004).

To address this limitation, this study employs the continuous wavelet transform (CWT) method for flux derivation.

The primary advantage of the CWT approach is that it does not require stationarity and eliminates the need for data detrending, thereby avoiding systematic errors that can arise from linear detrending procedures (Rannik and Vesala, 1999). This study follows CWT flux derivation method of (Torrence and Compo, 1998), described below.

The wavelet coefficient, $W_N(a, b)$, for a function $x(z)$ which changes with height, is calculated as a function of both location (height for airborne measurements or time for ground-based measurements) and scale (frequency or wavenumber) through convolution with a wavelet function (ψ):

$$W_N(a, b) = \int_{-\infty}^{\infty} x(z) \psi_{a,b}(z) dz \quad (1)$$

Deleted: However, a high correlation coefficient alone does not determine the precise temporal offset between the two signals. C

Deleted: ¶

2.3.2 Time lag correction ¶

Accurate temporal alignment is critical for flux computations when data originate from multiple instruments in field campaigns. For tower-based or surface measurement systems, temporal synchronization typically employs cross-correlation analysis in which the vertical velocity time series is temporarily shifted (forward or backward) relative to the particle concentration time series (Stull, 1988). Although inlets are usually positioned in close proximity to sample identical air masses, this temporal adjustment is necessary to account for potential transport delays to detectors, which are often located at different positions on the tower. This approach operates on the principle that flux calculations (cross-correlation values) reach their maximum when both signals are optimally synchronized, thereby enabling accurate lag time determination. Similar analysis is essential for aircraft data processing to account for both signal delay (when inlets share the same location, but detectors are positioned differently) and spatial separation effects (when inlets themselves are located at different positions on the aircraft). ¶

Platform-Specific Measurement Characteristics: Flux measurements differ fundamentally between tower-based and aircraft platforms in their spatial and temporal sampling characteristics. Tower measurements provide continuous observations at fixed heights, capturing the complete turbulent eddy spectrum within the atmospheric boundary layer, including low-frequency contributions essential for accurate flux estimates (Helbig et al., 2021; Sakai et al., 2001). Aircraft measurements sample different air masses as the platform moves horizontally, effectively trading temporal for spatial averaging (Desjardins et al., 1989). Aircraft measurements at higher boundary layer altitudes face additional challenges. In convective boundary layers, turbulent intensity increases with height above the surface layer before decreasing after $0.3\text{--}0.4 z_i$ (where z_i is the boundary layer height), requiring measurement lengths of 100 to 10^4 times the boundary layer height to maintain flux variance within 10% (Lenschow and Stankov, 1986). For aircraft traveling at 100 m s^{-1} , a 10 Hz sampling system resolves eddies as small as 20 m, while a 1 Hz sampling system resolves eddies down to 200 m. ¶

Tower measurements easily satisfy stationarity requirements through 30-minute averaging periods, whereas aircraft measure turbulence over large areas much faster but must assume spatial homogeneity along the flight path (Gioli et al., 2004). High aircraft speeds introduce additional constraints on sensor response times and spatial resolution, as instruments must respond quickly enough to resolve the smallest relevant eddies, a challenge that intensifies at higher flight speeds and lower altitudes where smaller eddy sizes result in higher observed frequencies when sampled by fast-moving aircraft (Desjardins et al., 1989) ¶

CPC synchronization validation: Since the CPCs used in this study were connected to the same isokinetic inlet from different positions, confirmation was needed that they sampled identical air masses (... [1])

Deleted: ¶

¶

Deleted: over traditional methods

Deleted: conditions

Deleted: preventing

Deleted: in flux calculations

Deleted: the method

Deleted: of

Deleted: for CWT flux derivation

Deleted:

418 where (z) represents the wavelet function, controlled by the scale parameter (a) and translation parameter (b) . The
 419 scale parameter governs the wavelet frequency, while the translation parameter shifts it in the temporal domain. The
 420 wavelet function is defined as:

$$421 \quad \psi_{a,b}(z) = \frac{1}{\sqrt{a}} \psi_0\left(\frac{z-b}{a}\right) \quad (2)$$

Deleted:

422 All wavelet functions are based on a “mother” wavelet. For this study, the Morlet wavelet is chosen as the mother
 423 wavelet, which is the product of a plane wave with a Gaussian function (Torrence and Compo, 1998). Schaller et al.,
 424 (2017) reported that the Morlet wavelet provides reliable results in flux analysis even when traditional eddy covariance
 425 methods fail.

$$426 \quad \psi_0(\eta) = \pi^{-\frac{1}{4}} e^{i\omega_0\eta} e^{-\frac{\eta^2}{2}} \quad (3)$$

Deleted:

427 where ω_0 is the non-dimensional frequency (set to 6 for this study), and η is the non-dimensional time parameter and
 428 , the first exponential term is the complex sinusoid, and the second exponential term is the Gaussian envelope. Using
 429 this methodology, the vertical turbulent particle flux can be calculated according to (Schaller et al., 2017; Torrence
 430 and Compo, 1998) as:

Deleted: -

Deleted: -

$$431 \quad \overline{w'(z)N'_{3-10}(z)} = \frac{\delta t}{c_s} \times \frac{\delta_j}{L} \times \sum_{n=0}^{L-1} \sum_{j=0}^J \left[\frac{W_N(a,b) \times W_w^*(a,b)}{a(j)} \right] \quad (4)$$

Deleted:

432 c_s , the wavelet specific reconstruction factor is taken as 0.776, which is empirically derived for the chosen wavelet
 433 (Schaller et al., 2017; Torrence and Compo, 1998), L represents the number of elements in the time series with
 434 timestep δ , which is the inverse of frequency (1 Hz for this study), J is the maximum number of scales with δ_j being
 435 the space between each discrete scale (Schaller et al., 2017; Torrence and Compo, 1998).

$$436 \quad J = \delta_j^{-1} \times \log_2\left(\frac{L \times \delta t}{s_0}\right) \quad (5)$$

437 δ_j was chosen to be 0.25 s (Schaller et al., 2017; Torrence and Compo, 1998), this value can be adjusted to get better
 438 scale resolution at the expense of higher computational cost, s_0 is the smallest scale of the wavelet taken as 2δ , $a(j)$ is
 439 the scale parameter for the discrete scale calculated as:

$$440 \quad a(j) = s_0 \times 2^{j\delta_j} \quad j = 0, 1, \dots, J \quad (6)$$

Deleted:

441 $W_N(a,b)$ is the wavelet coefficient for the particle concentration signal, and $W_w^*(a,b)$ is the complex conjugate of the
 442 wavelet coefficient for the vertical velocity signal. Under stationary conditions, fluxes calculated using both CWT and
 443 traditional eddy covariance methods should yield equivalent results, though agreement may vary in aircraft
 444 measurements due to the presence of non-stationarities (Misztal et al., 2014; Wolfe et al., 2018).

451 **2.5 Limit of Detection Determination**

452 Spirig et al., (2005) demonstrated that calculating covariance at time ranges significantly larger than the integral time
453 scale can quantify the precision of individual flux determinations. ~~The integral time scale was calculated using the~~
454 ~~cross-correlation function between vertical wind w and 3-10 nm sized particle size concentration, using the method~~
455 ~~described by (Lenschow et al., 2000; Wulfmeyer et al., 2016). The cross covariance is given as:~~

456 $A_{x,y}(\tau) = \text{cov}(x_t, y_{t+\tau})$ (7)

457 ~~Where x_t and y_t are the two signals of interest, with y shifted by the lag time τ . Now the cross covariance is fitted to a~~
458 ~~model of the form:~~

459 $A_{\text{model}}(\tau) = v - k\tau^2$ (8)

460 ~~Where v and k are fitted parameters. The line is fitted till the first zero crossing of the cross covariance. And using this~~
461 ~~the integral timescale, I is calculated as:~~

462 $I = \frac{2}{5} \left(\frac{v}{k} \right)^{3/2}$ (9)

463 ~~The median value of the integral timescale for the flux events was ~ 11 seconds. The limit of detection (LoD) is~~
464 ~~defined as 1.96 times (95% confidence interval) the standard deviation of covariance between w and N_{3-10} when one~~
465 ~~of the signals is temporarily shifted with respect to the other. To estimate the precision of an individual flux~~
466 ~~determination, we followed Spirig et al. (2005) and examined fluctuation of the covariance function at time lags far~~
467 ~~away from the true lag. The standard deviations of the covariance function were calculated between 4500 to 5700~~
468 ~~seconds (corresponding to 45 to 57 km spatial displacement) before and after the peak fluxes. These lag times were~~
469 ~~selected to be much higher than the integral timescale of turbulence at all measurement heights. The limit of detection~~
470 ~~(LoD) is defined as 1.96 times (95% confidence interval) the standard deviation of covariance between w and N_{3-10}~~
471 ~~when one of the signals is temporarily shifted with respect to the other. Signal shifts -10 to $+10$ seconds~~
472 ~~(corresponding to ± 1 km spatial displacement) are applied to ensure complete decoupling between the signals. Flux~~
473 ~~calculations are restricted to periods when the aircraft maintained horizontal, straight line flight segments to ensure~~
474 ~~reliable flux estimates and minimize the influence of aircraft maneuvers on turbulence measurements. The limit of~~
475 ~~detection is used as an absolute value and hence if a particular flux event is lower in absolute value compared to the~~
476 ~~LoD, they will not be considered for analysis.~~

477 **2.6 Small particle events selection criteria**

478 Establishing appropriate threshold values for new particle formation over tropical oceanic regions presents significant
479 challenges due to sparse observational datasets and the intricate interactions between meteorological and chemical
480 processes in these environments. Earlier studies have typically used concentration thresholds of 10^3 to 10^4 particles
481 cm^{-3} for ultrafine particles (3–25 nm) to distinguish nucleation events from background conditions. However, these
482 criteria were primarily established based on observations from continental or mid-latitude marine environments (Dal
483 Maso et al., 2005; Kulmala et al., 2012). Given that tropical marine regions are characterized by reduced background
484 aerosol loadings and distinct precursor gas profiles relative to higher latitude zones, more conservative thresholds

Formatted: Font color: Blue

Formatted: Font color: Blue

Formatted: Font color: Blue

Formatted: Font color: Blue

Formatted: Font color: Blue

Formatted: Font color: Blue, Subscript

Formatted: Font color: Blue, Subscript

Formatted: Font color: Blue

Formatted: Default Paragraph Font, Font: Not Bold, English (UK)

Formatted: Font color: Blue

Deleted: Since the integral time scale cannot be accurately determined in this study, we employ a large time range approach

Formatted: Line spacing: 1.5 lines

Deleted: (Dal Maso et al., 2005; Kulmala et al., 2012)

488 (500–1000 particles cm^{-3}) may prove better suited for detecting nucleation phenomena in these relatively unpolluted
 489 environments (Modini et al., 2009; Weber et al., 1997). Additionally, the aircraft-based measurement method
 490 prevented the implementation of traditional nucleation event identification criteria, specifically the requirement for
 491 persistent concentration increases spanning 1–2 hours to distinguish genuine nucleation from brief local source
 492 influences (Kulmala et al., 2012).

493 For this study, we modified the methodology established by Zheng et al., (2021) to detect small particle
 494 events (SPEs). Individual 1-second measurements were used to identify when N_{3-10} concentrations exceeded 150 cm^{-3} ,
 495 once identified the measurements that exceeded the threshold were grouped into 10-second intervals (equivalent to ~ 1
 496 km spatial resolution), and the average N_{3-10} for the group was checked to see if it achieved statistical significance
 497 using:

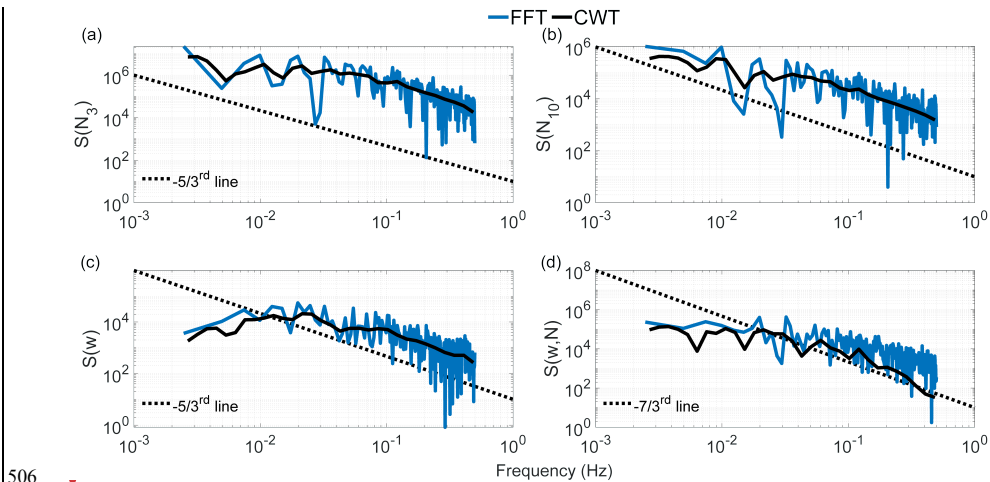
498
$$N_3 - N_{10} > 3\sigma_D$$

499 where σ_D represents the uncertainty in the concentration difference between N_3 and N_{10} , expressed as:

500
$$\sigma_D = \sigma(N_3 - N_{10})$$

501 **2.7 Frequency response and flux averaging time**

502 Momentum, enthalpy, and matter are transported in the atmosphere by eddies of different spatial scales. One-
 503 dimensional power spectral analysis is used to decompose the signal into components of different frequencies, which
 504 are associated with different eddy sizes. Fast Fourier Transform (FFT) and Continuous Wavelet Transform (CWT)
 505 were used to calculate the power spectral density (PSD) of vertical wind speed and particle concentration.



506

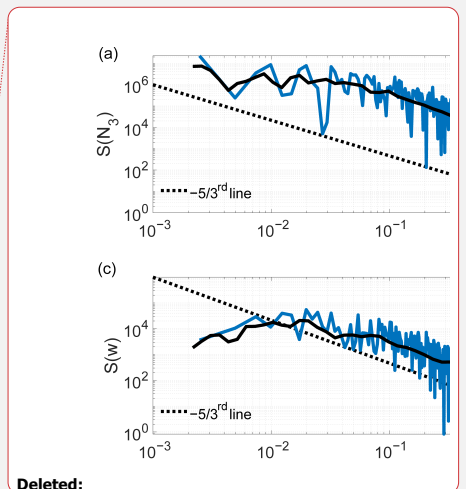
(10)

Deleted: 7

(11)

Deleted: 8

Formatted: Line spacing: 1.5 lines



Deleted:

510 **Figure 1. Power spectral density for (a) N_3 , (b) N_{10} , (c) vertical wind velocity, and (d) 3-10 nm particle flux.**

511 Figure 1 shows the PSD for a flight leg on 21 June 2017 between 13:43 and 13:49 UTC at a height of 550 m above
512 mean sea level. Dashed lines represent the theoretical slopes for the inertial subrange, which describe how energy
513 cascades from larger to smaller eddies and finally dissipates as heat due to viscous friction (Pope, 2000). Both particle
514 concentration spectra (Figs. 1a,b) and the flux spectrum (Fig. 1d) broadly follow the theoretical $-5/3$ and $-7/3$
515 Kolmogorov scaling across the resolved frequency range. The supplementary figure comparing 1 Hz and 10 Hz
516 vertical wind velocity spectra (Supplementary Fig. S7) confirms that turbulent energy exists at scales beyond the 1 Hz
517 Nyquist frequency. The absence of a visible noise floor in the particle concentration spectra at high frequencies reflects
518 the band-limited response of the CPC, which acts as a low-pass filter that attenuates high-frequency concentration
519 fluctuations, producing a steep spectral roll-off rather than a white noise floor. While this results in a cleaner spectrum
520 visually, it still represents real flux loss at high frequencies that is accounted for through the correction described in
521 Section 2.8.

522
523 Figure 1 also shows some differences between FFT and CWT flux calculations, especially for fluxes at high
524 frequencies. These differences are attributable primarily to non-stationarity in the aircraft data, as the platform moves
525 through different air masses, meteorological conditions, and altitudes. FFT assumes stationarity over the entire
526 analysis window and can therefore introduce artifacts under such conditions, whereas CWT provides time-localized
527 frequency information that is more robust for non-stationary signals (Schaller et al., 2017). Li et al., (2023) evaluated
528 uncertainties of turbulent flux calculation using both methods, finding that biases can range from 50–100% of the
529 spectrally complete flux. We note that the high-frequency deviations visible in the particle concentration spectra are
530 not a consequence of FFT limitations but reflect the band-limited response of the CPC, which attenuates concentration
531 fluctuations at frequencies above ~ 0.3 Hz, as discussed in Section 2.8. The CWT's more conservative high-frequency
532 response may better represent the actual resolvable flux contributions (Misztal et al., 2014).

533 To assess whether the calculated fluxes adequately represent both low- and high-frequency turbulent contributions,
534 we conducted ogive analysis using the approach described by Foken et al., (2006). Mobile measurement platforms
535 necessitate modified considerations for flux averaging intervals. Standard 30-minute averaging periods used in
536 stationary tower observations are inappropriate for aircraft measurements. Considering the aircraft's ground speed, a
537 90-second sampling period covers an equivalent air mass to that sampled by a stationary sensor over 30 minutes at
538 typical wind speeds of 5 m s^{-1} . To enable direct comparison between ogives computed using FFT and CWT methods,
539 normalization was applied according to Sun et al., (2018):

$$540 \sigma_g(f) = \frac{og(f)}{sgn(\max(og(f)) + \min(og(f))) \max(|og(k)|)} \quad (12)$$

541 where $sgn\{x\}$ represents the signum function, returning +1 for positive x , -1 for negative x , and zero when x equals
542 zero. When the normalized ogive equals 1, the ogive value corresponds precisely to the covariance value for that
543 averaging period. The advantage of this normalization approach is that it facilitates the identification of cases where
544 low-frequency turbulence has an opposite sign to high-frequency turbulence. In such situations, large and small eddies
545 transport material in opposing directions, indicating complex atmospheric processes such as counter-gradient

Formatted: Space After: 12 pt

Deleted: ¶

Deleted: Both particle concentration spectra (e.g., Fig. 1b) and flux spectra (Fig. 1d) exhibit deviations from the theoretical $-5/3$ and $-7/3$ Kolmogorov scaling at frequencies larger than 0.3 Hz. The spectral flattening observed at these frequencies is characteristic of white noise, suggesting instrumental limitations where the CPC cannot adequately resolve concentration fluctuations faster than ~ 3 sec.

Deleted: likely stem from several key methodological differences. Aircraft data are inherently non-stationary as the platform moves through different air masses, meteorological conditions, and altitudes. FFT assumes stationarity over the entire analysis window, which can introduce artifacts at high frequencies when applied to non-stationary aircraft data. CWT can handle non-stationary signals by providing time-localized frequency information, making it more robust for aircraft measurements (Schaller et al., 2017).

Deleted: eddy covariance and wavelet analysis

Deleted: "EC and Morlet-wavelet generate

Deleted: ranging

Deleted: 'true'

Deleted: values

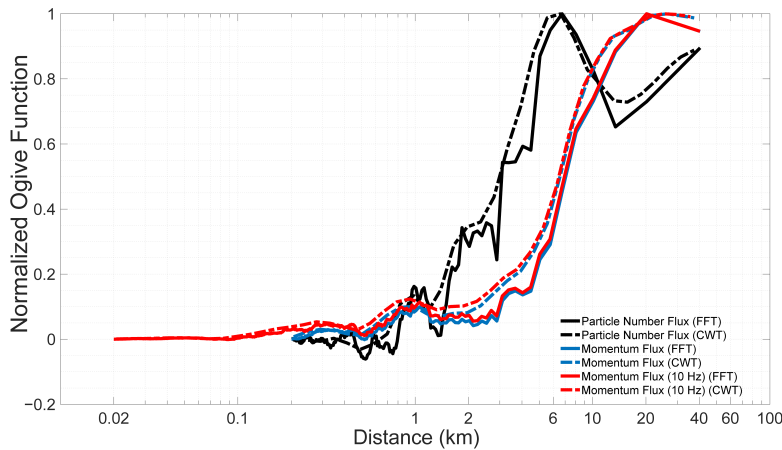
Deleted: FFT can suffer from spectral leakage, especially at high frequencies, when the raw signal doesn't fit perfectly into the sine or cosine signal in the analysis window. This is particularly problematic for aircraft data, where turbulent structures may not be periodic over the sampling interval (Harris, 1978). CWT uses wavelets that are naturally windowed and localized, reducing leakage effects. ...

Formatted: Font color: Blue

Deleted: At high frequencies corresponding to small spatial scales, aircraft measurements become increasingly challenging due to sensor response time limitations, spatial averaging effects, and platform motion artifacts (more on this in Sect. 2.8).

Deleted: ¶

579 transport. The normalized ogive plot visually reveals these opposing contributions through characteristic rise-and-fall
 580 patterns that might otherwise be obscured in non-normalized data.
 581 Figure 2 illustrates the ogive as a function of distance covered by the aircraft for the same flight leg shown in Fig. 1.
 582 Signal frequency was converted to distance by dividing the aircraft speed (assumed to be constant at 100 m s^{-1}) by the
 583 frequency obtained from the FFT or CWT analysis. This plot reveals that the particle flux for this flight leg can be
 584 resolved by averaging over 40 km. While both FFT and CWT ogives show agreement for this case, such consistency
 585 cannot be expected universally; therefore, CWT fluxes are used throughout this study for the reasons discussed in
 586 previous sections.



587

588 **Figure 2: Normalized ogive function as a function of distance covered by the aircraft. The ogive represents the cumulative**
 589 **fractional contribution to total flux from high to low frequencies.**

Deleted: Normalized ogive function.

590 2.8 Flux loss correction

591 If the sensor used to measure fluxes are too slow to accurately capture the smaller eddies that contribute to the total
 592 flux, the turbulent fluxes will require correction. For micrometeorological flux measurements on towers at 10 m above
 593 the surface, instruments are typically operated at 10 Hz (Nyquist frequency = 5 Hz). Under typical wind speeds of 5
 594 m s^{-1} , this sampling rate can resolve eddies as small as $\sim 1 \text{ m}$, ensuring that most energy-containing and inertial
 595 subrange eddies are captured (Aubinet et al., 2012; Lee et al., 2005; Stull, 1988).

596 However, airborne flux measurements present different challenges. The integral length scales of turbulent eddies
 597 increase approximately linearly with height within the surface layer (roughly the bottom 10% of the boundary layer),
 598 then remain approximately constant above this level, limited by the boundary layer height (Kaimal and Finnigan,
 599 1994). In the mixed layer portion of a typical boundary layer (above $\sim 100 \text{ m}$ surface layer), integral length scales are
 600 typically 100-200 m (Lenschow and Stankov, 1986). At an aircraft ground speed of 100 m s^{-1} , the 1 Hz sampling
 601 provides 200 m spatial resolution, which approaches but does not fully resolve the integral length scale. Consequently,

603 the sampling resolution approaches the lower limit for adequately resolving the dominant flux-carrying scales and
604 may under sample contributions from smaller turbulent structures.

605 To address this limitation, we applied the approximations from Horst (1997) to estimate the ratio of measured flux
606 (F_m) to spectrally complete flux (F) for different atmospheric stability conditions encountered during campaign flights:

$$607 \frac{F_m}{F} = \frac{1}{1 + (2\pi n_m \tau_c \frac{u}{z})^\alpha} \quad (13)$$

608 where F_m is the measured flux, F is the spectrally complete flux, u is the magnitude of average wind speed, z is the
609 height of the airplane, τ_c is the response time constant of the CPC, which was taken as 3.0 s, $\alpha =$ seven-eights- and n_m
610 $= 0.085$ for neutral and unstable conditions (Pryor et al., 2007). Equation 13 was originally developed by Horst (1997)
611 to estimate the attenuation of scalar flux measurements within the surface layer, but has been applied to aircraft
612 measurements (Gioli et al., 2004), with corrected airborne fluxes showing good agreement with tower data when
613 aircraft measurements were conducted over homogeneous surfaces at altitudes comparable to tower height.

614 To illustrate the practical importance of this correction, the $\frac{F_m}{F}$ ratio varies substantially depending on measurement
615 height and atmospheric stability conditions encountered during the campaign. For measurements conducted near the
616 top of the marine boundary layer (~1,200–1,400 m) under near-neutral to unstable conditions, $\frac{F_m}{F}$ values approach
617 unity (0.93–0.99), indicating that flux losses are modest at these heights where the dominant flux-carrying eddies are
618 large relative to the CPC response limitation. However, for measurements conducted closer to the surface (~30–550
619 m), $\frac{F_m}{F}$ values range from 0.70 to 0.95, implying that uncorrected fluxes could underestimate the spectrally complete
620 flux by up to 30%. This highlights the importance of applying the flux loss correction, particularly for low-altitude
621 flight legs where eddy sizes are smaller and the CPC response time constant becomes a more significant fraction of
622 the dominant flux-carrying eddy turnover times.

623 Following the approach of Islam et al., (2022), we assessed the random uncertainty in particle flux due to counting
624 statistics. We found it to be 2–3 orders of magnitude lower compared to the measured flux magnitudes reported in this
625 study. Therefore, the correction due to discrete counting statistics of CPCs was not applied to this study.

626 3.0 Results

627 We examine two flight days as case studies of SPEs observed at varying altitudes above the ocean. Additional
628 supporting flights are presented in the Supplementary Information. Table 1 summarizes the N_{3-10} vertical turbulent
629 flux estimates derived from all six flight days analyzed in this study, grouped by the inferred nucleation regime. Flights
630 1 and 2 (January 29 and February 10, 2018) are classified as entrainment zone nucleation events, where SPEs were
631 detected near the top of the MBL at heights exceeding 1,200 m. Flights 3–6 (June 21 and July 7, 2017; February 18
632 and 12, 2018) are classified as decoupled layer nucleation events, with SPEs observed across a broader range of
633 altitudes (30–837 m). For all events, the ratio of measured flux to the spectrally complete flux ($\frac{F_m}{F}$) exceeds 0.76,
634 indicating minimal flux loss due to sensor response limitations. The normalized vertical velocity variance ($\sigma_w^2 w_*^{-2}$)
635 is generally low, consistent with relatively quiescent turbulent conditions during the measurement periods. Negative

Deleted: "true"

Deleted:

Deleted: 0

Deleted: "true"


Deleted: 10

Formatted: Font color: Blue

Deleted: We examine two flight days as case studies of SPEs observed at varying altitudes above the ocean. Additional supporting flights are presented in the Supplementary Information for each case

644 flux values indicate downward transport of freshly nucleated particles from the entrainment zone toward the surface,
 645 while positive values suggest upward transport from a source within the decoupled sub-cloud layer. Two of these
 646 flight days, January 29, 2018 (Case 1) and June 21, 2017 (Case 2), are examined in detail as case studies in the
 647 following sections, with the remaining four flights presented as supporting examples in the Supplementary
 648 Information. **Table 1. Summary of N_{3-10} particle vertical turbulent flux estimates from aircraft campaigns with**
 649 **detection limits and flux loss assessment.**

No	Date	Time (UTC)	Height (m)	N_{3-10} flux ($\text{cm}^{-2} \text{s}^{-1}$)	LoD ($\text{cm}^{-2} \text{s}^{-1}$)	F_m/F	$\sigma^2 w^{-2}$
Entrainment zone nucleation							
1	01/29/18	10:54:59-10:58:13	1,205	-41,092	34,423	0.97	0.01
		12:18:47-12:21:50	1,218	-2,975	2,085	0.98	0.005
2	02/10/18	13:53:20-13:55:02	1,375	-1,195	381	0.93	0.003
Decoupled layer nucleation							
3	06/21/17	14:03:30-14:09:25	800	1,139	294	0.99	0.016
		13:56:10-14:02:25	800	2,929	1,239	0.98	0.021
		13:42:40-13:49:23	550	-2,782	1,995	0.95	0.1

Deleted: 
 Table 1. Summary of N_{3-10} particle vertical turbulent flux estimates from aircraft campaigns with detection limits and flux loss assessment. ...

		13:32:20-13:38:40	30	-860	400	0.76	0.17
4	07/07/17	13:42:18-13:43:04	565	-94,093	49,410	0.86	0.02
		13:43:07-13:44:58	535	-21,317	4,959	0.90	0.031
5	02/18/18	14:17:32-14:19:38	555	298	115	0.81	0.016
		14:47:10-14:51:34	250	-3,217	1,153	0.70	0.056
6	02/12/18	14:54:27-14:58:37	837	5,433	1,173	0.93	0.04

654 **Case 1: SPE occurring in the entrainment zone near the top of the marine boundary layer**

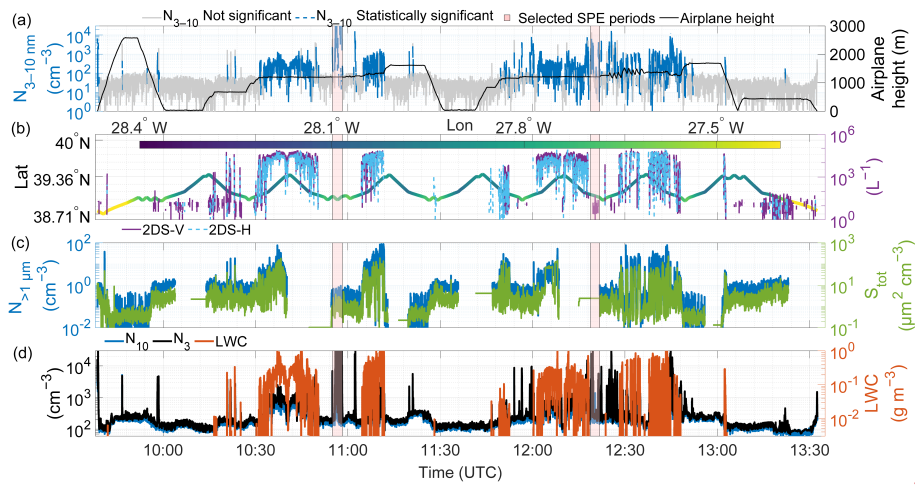
655 [Figures 3–5](#) present data collected on January 29, 2018 with an additional example from February 10, 2018, shown in
656 [Supplementary Figs. S8–S10](#). Back-trajectory analysis (not shown) indicates that the sampled airmasses had been
657 circulating around the Azores for the preceding three days and were therefore likely less polluted than North American
658 outflow air masses. Figure 3 shows a multi-panel time series covering approximately 3.5 hours of flight operations.
659 The aircraft initially ascended to ~2,500 m but generally remained below ~1,500 m for most of the flight (Fig. 3a).
660 The flight trajectory (Fig. 3b) reflects predominantly east-west movement across the Azores region, spanning latitudes
661 from approximately 38.7° to 39.4°N and longitudes from -28.4° to -27.4°W. Drizzle number concentration measured
662 by 2DS (purple and blue lines in Fig. 3b) was absent or low during the selected SPE periods. Elevated drizzle number
663 concentration, together with high liquid water content regions (orange in Fig. 3d), mark frequent cloud encounters.
664 Following our quality control procedures, all N_{3-10} concentration data with $LWC \geq 3 \times 10^{-3} \text{ g m}^{-3}$ were excluded from
665 analysis to avoid contamination from cloud droplet shattering artifacts. Pink-shaded periods mark the intervals chosen
666 for detailed analysis, which exhibited simultaneous increases in both N_3 and N_{10} concentrations exceeding 10^4 cm^{-3}
667 (indicating an SPE). Supermicron particle concentration (blue in Fig. 3c) as well as total particle surface area (green
668 in Fig. 3c) were also low during the selected SPE periods, indicating the absence of particles such as sea spray aerosols.
669

Formatted: Font color: Blue

Deleted: 7

Deleted: 9

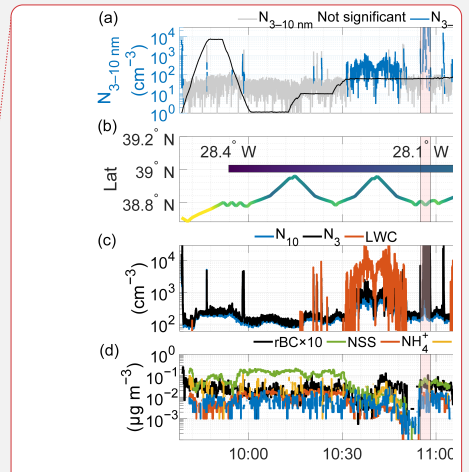
Formatted: Font color: Blue



672

673
674
675
676

Figure 3. Multi-parameter time series from the January 29, 2018 flight. (a) N_{3-10} particle concentrations and aircraft altitude; (b) aircraft position (latitude and longitude) and drizzle number concentration; (c) supermicron particle concentration and total particle surface area (S_{tot}); (d) particle number concentrations (N_{10} and N_3) and liquid water content. Gaps in the time series indicate the missing data.



Deleted:

Formatted: Font: 9 pt, Font color: Blue

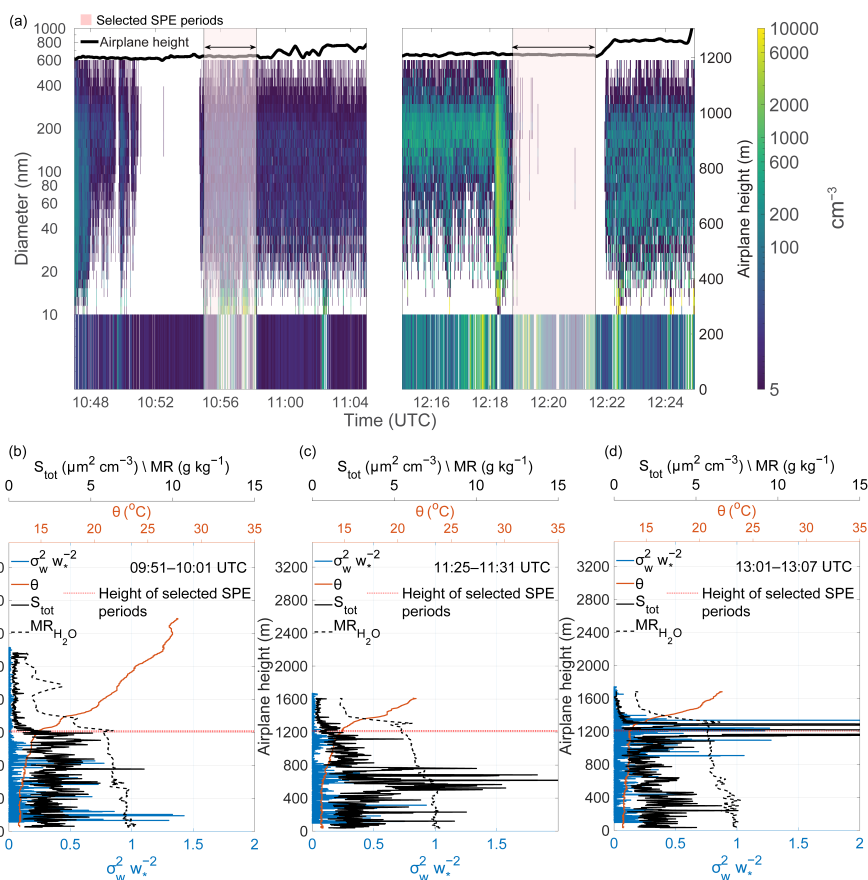
Formatted: Font: 9 pt

Formatted: Font: 9 pt

Formatted: Font: 9 pt

Formatted: Font: 9 pt, Font color: Blue, English (US)

Formatted: Font: 9 pt, Font color: Blue



678

679 **Figure 4. (a) Size-resolved particle number concentrations (10–600 nm) from FIMS as a function of time and altitude, with**
 680 **N_{3-10} concentrations shown in the lower strip. Pink shading indicates selected SPE periods. (b-d) Vertical profiles of**
 681 **potential temperature (θ), normalized vertical velocity variance ($\sigma_w^2 w_*^{-2}$), total particle surface area (S_{tot}), and water vapor**
 682 **mixing ratio (MR_{H_2O}) for three time periods nearest to the selected SPE periods: (b) 09:51–10:01 UTC, (c) 11:25–11:31**
 683 **UTC, and (d) 13:01–13:07 UTC. Gaps in the time series indicate the missing data.**

684

685 Figure 4a shows the temporal evolution of particle concentration between ~10:47–11:05 and ~12:15–12:25 UTC. The
 686 colormap represents FIMS-derived, size-resolved aerosol number concentrations (10–600 nm diameter), varying
 687 across time and altitude, while the lower panel displays N_{3-10} concentrations. The two pink-highlighted intervals are
 688 the same as in Fig. 3. The high particle concentration spike observed ~12:18 UTC coincides with elevated LWC and
 689 drizzle concentration (Fig. 3d) and was excluded from analysis following our quality control procedures (Section
 690 2.3.1). Weber et al. (1998) documented that cloud droplet shattering can produce artifactual particle concentrations as

Deleted: Figure 3. Multi-parameter time series during the January 29, 2018 flight showing: (a) N_{3-10} particle concentrations with aircraft altitude (b) aircraft position with latitude and longitude; (c) particle number concentrations for N_{10} , N_{3} , and liquid water content; and (d) non-refractory aerosol chemical composition including non-seasalt sulfate (NSS), ammonium (NH_4^+), organics (Org), chlorine ion (Cl^-), refractory black carbon (rBC, multiplied by 10 for visualization) in $\mu g m^{-3}$, and trace gases dimethylsulfide (DMS) and methanol in ppbv. Figure 3 presents a multi-panel time series spanning approximately 3.5 hours of flight operations. The aircraft first ascended to ~2,500 m but generally operated below ~1,500 m throughout the flight (Fig. 3a). The flight trajectory (Fig. 3b) demonstrates predominantly east-west movement across the Azores region, spanning latitudes from approximately 39.0° to 39.5°N and longitudes from ~28.4° to ~27.4°W. High liquid water content regions (orange in Fig. 3c) indicate frequent cloud encounters. Following our quality control procedures, all N_{3-10} concentration data with liquid water presence were excluded from analysis to prevent contamination from cloud droplet shattering artifacts. The pink-shaded periods mark the intervals chosen for detailed analysis, which exhibited simultaneous increases in both N_3 and N_{10} concentrations exceeding $10^6 cm^{-3}$ (indicating an SPE). Figure 3d demonstrates that these periods contained no measurable liquid water and were distinguished by substantial concentrations (~0.1 $\mu g m^{-3}$) of non-seasalt sulfate. Organic concentrations were also elevated throughout the flight, especially during the second half.

Deleted: Figure 4. (a) The main panel shows size-resolved particle number concentrations (10–600 nm) from FIMS as a function of time and altitude, while N_{3-10} concentrations in the lower strip. (b-d) Vertical profiles of potential temperature (θ), normalized vertical velocity variance ($\sigma_w^2 w_*^{-2}$), particle total surface area (S_{tot}), and water vapor mixing ratio (MR). Gaps in the time series indicate the missing data.

725 small as 3 nm in airborne CPC measurements, making this the most plausible explanation for the observed spike.
726 Aircraft exhaust contamination can be ruled out, as the nearest prior flight transect over this region occurred
727 approximately half an hour earlier at an altitude ~60 m lower, more than sufficient time and vertical separation for
728 complete plume dispersal. This data point was therefore excluded from all flux calculations as the concurrent LWC
729 exceeded the quality control threshold of $3 \times 10^{-3} \text{ g m}^{-3}$.

730 Figures 4b–d present vertical profiles of potential temperature, normalized vertical velocity variance ($\sigma_w^2 w_*^{-2}$) i.e.,
731 (the vertical velocity variance normalized by the square of the convective velocity scale), total particle surface area,
732 and the water vapor mixing ratio at three locations nearest to the pink-highlighted intervals. Sharp gradients in the
733 potential temperature (orange) mark the top of the MBL, defining the capping inversion that suppresses vertical mixing
734 between the boundary layer and the free troposphere. The co-occurrence of these temperature gradients with elevated
735 normalized vertical velocity variance ($\sigma_w^2 w_*^{-2}$) near the inversion level indicates the presence of an entrainment zone,
736 where thermodynamic forcing (including cloud-top radiative cooling and wind shear) drives mixing between the free
737 tropospheric air above and the convective boundary layer below (Boers and Eloranta, 1986). Figures 4b–d reveal a
738 deep boundary layer with the entrainment zone between approximately 1,200–1,400 m, consistent with previous
739 estimates that entrainment zones typically comprise 20–40% of boundary layer depth (Martin et al., 2014).

740 Figures 4b–d present the profiles of ($\sigma_w^2 w_*^{-2}$) profiles, a metric that characterizes the intensity of turbulent structures
741 in convective boundary layers (Deardorff, 1974; Dewani et al., 2023). These profiles show elevated ($\sigma_w^2 w_*^{-2}$) values
742 near the ocean surface and within the entrainment zone, with minimal values in the free troposphere, where significant
743 turbulence is absent.

744 The water vapor mixing ratio profiles in Figs. 4b–d reveal evolving boundary layer moisture structure during the
745 flight. The early profile (Fig. 4b) shows a relatively well-mixed moisture distribution below the capping inversion at
746 ~1,200 m, with a sharp decrease into the drier free troposphere above. The latter profiles (Figs. 4c–d) exhibit a two-
747 step moisture structure, with a sharper gradient near ~600 m suggesting progressive decoupling of the boundary layer
748 during the course of the flight, separating a moister surface layer from a drier sub-cloud layer above. Despite some

749 vertical variability shown in Figs. 4b–d, the total particle surface area (S_{tot}) remained relatively low throughout the
750 flight, falling well below the campaign averages of $\sim 30 \mu\text{m}^2 \text{ cm}^{-3}$ in the surface mixed layer and $\sim 10 \mu\text{m}^2 \text{ cm}^{-3}$ in the
751 upper decoupled layer reported by Zheng et al. (2021). Figure 4c also shows a distinct S_{tot} maximum at an altitude
752 where small gradients in both potential temperature and mixing ratio suggest the presence of an entrainment layer.
753 The pronounced S_{tot} increase could indicate a nucleation occurring at this location (see Case 2 below), although this
754 hypothesis could not be independently verified looking at the N_{3-10} data in this case. Figure 4c shows that the
755 entrainment zone and free troposphere were characterized with extremely low S_{tot} values.

756 Figure 5 presents the spatial distribution of N_{3-10} particle concentrations along the flight path at ~1,200 m altitude
757 (dashed lines in Figs. 4b–d), with the calculated vertical turbulent fluxes labeled at their respective measurement
758 locations. Concentrations up to $10,000 \text{ cm}^{-3}$ were observed along the flight track, with the highest values concentrated
759 within a horizontal extent of less than 10 km. The substantial downward fluxes of N_{3-10} particles ($-41,092$ and $-2,975$
760 $\text{cm}^{-2} \text{ s}^{-1}$) at ~1,200 m both exceed their respective limits of detection (Table 1), confirming that the observed downward
761 transport represents a statistically significant atmospheric signal rather than measurement noise. The downward flux

Deleted: is likely an artifact due to cloud droplet shattering.

Formatted: Font color: Blue

Formatted: Font color: Blue

Formatted: Font color: Blue

Deleted: (Sharp gradients in the potential temperature (orange) profile, often called potential temperature inversion or capping inversion, mark the top of the MBL. These gradients indicate the presence of an entrainment zone (e.g.,

Deleted: , a layer at the top of the boundary layer where free tropospheric air masses are entrained into the capping inversion and interact with convective thermals rising from below

Deleted: The sharp gradients in mixing ratios shown in Figs. 4b–d indicate moisture convergence that either precedes cloud formation or reflects recently dissipated clouds that have left behind residual moisture signatures due to changing atmospheric conditions. Figure 3 demonstrates frequent cloud encounters during this flight.

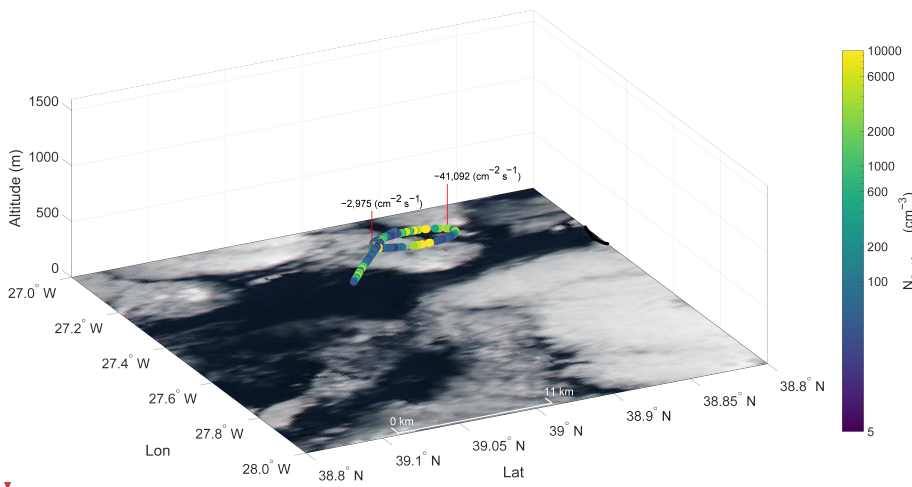
Deleted:

Deleted: ¶

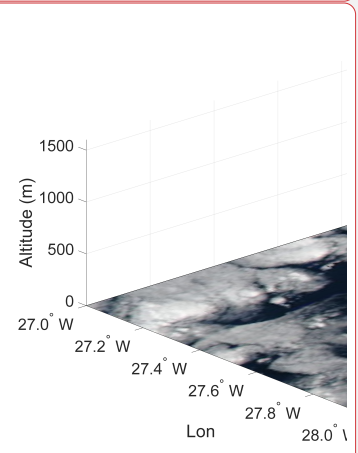
Deleted:

778 direction indicates that the source of freshly nucleated particles was located above the measurement altitude, within
 779 the entrainment zone, while the large difference in flux magnitudes between the two events likely reflects spatial
 780 heterogeneity in source strength and the proximity of the aircraft to the nucleation zone during each transect. This
 781 interpretation is supported by the near-absence of N_{3-10} at $\sim 1,600$ m during 11:14–11:25 and 12:51–13:01 UTC (Fig.
 782 3), with the exception of brief concentration spikes of uncertain origin retained in the record due to insufficient
 783 evidence for their removal. The small particle size (3–10 nm) and limited horizontal extent of less than 10 km further
 784 argue against a free tropospheric nucleation source, as particles originating in the free troposphere would be expected
 785 to have grown substantially and the plume to have diluted during descent to measurement altitude. Several mechanisms
 786 could promote nucleation specifically within the entrainment zone: adiabatic cooling in the rising convective plumes,
 787 turbulent fluctuation in temperature and vapor concentration generated by entrainment, and dilution of mixed-layer
 788 air by the entrained free tropospheric air, causing a sudden reduction in preexisting aerosol surface area (Nilsson et
 789 al., 2001). The extremely low S_{tot} values observed in the entrainment zone and free troposphere (Fig. 4), falling well
 790 below the campaign averages, are consistent with this interpretation. These conditions are analogous to those identified
 791 in previous studies linking entrainment zone nucleation to reduced condensation sink environments (Größ et al., 2018;
 792 Meskhidze et al., 2019; Nilsson et al., 2001). Supplementary Figs. S9 and S10 provide additional support, showing a
 793 downward flux of N_{3-10} particles ($-1,195 \text{ cm}^{-2} \text{ s}^{-1}$) at 1,375 m with complete absence of N_{3-10} above $\sim 1,400$ meters,
 794 consistent with SPE occurrence specifically within the entrainment zone between 1,375–1,400 m.
 795 Figures 3–5 and the flux analysis (Table 1) demonstrate that the entrainment zone nucleation near the MBL top
 796 occurred on two days (January 29 and February 10, 2018), representing nearly 5% of flight days. Despite a relatively
 797 small horizontal extent (<10 km), these newly formed particles can be entrained in the boundary layer via vertical
 798 turbulent processes, potentially playing an important role in marine aerosol number budget and, given sufficient time
 799 for growth to CCN-relevant sizes, potentially influencing cloud condensation nuclei concentrations for marine
 800 stratocumulus clouds.

- Deleted:** Previous studies identify the mixed layer or entrainment zone as the likely location for nucleation events
- Deleted:** that
- Deleted:** initiate
- Deleted:** include
- Deleted:** caused
- Deleted:** flux
- Deleted:** decrease
- Deleted:** concentration
- Deleted:** (Größ et al., 2018; Meskhidze et al., 2019; Nilsson et al., 2001)



Deleted: Combined with extremely low preexisting particle concentrations, these processes create favorable conditions for new particle formation. [†]



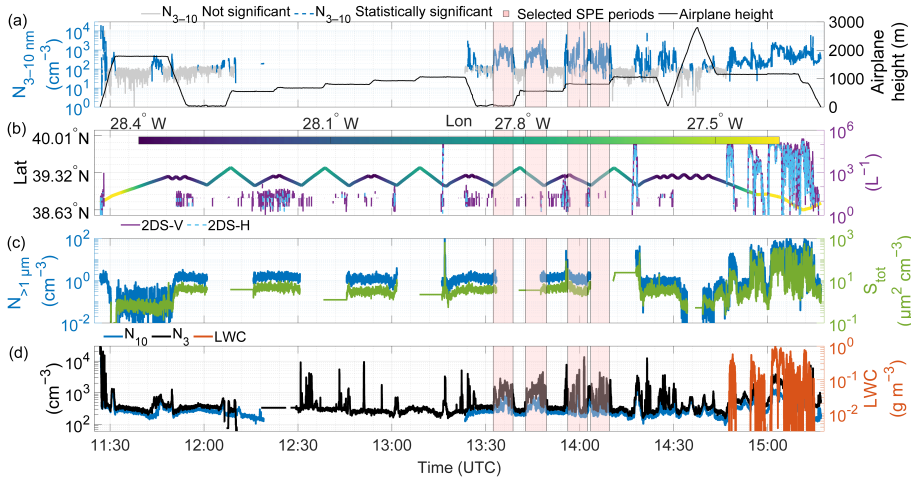
Deleted:

801

817 **Figure 5. Spatial distribution of N_{3-10} particle concentrations along the flight track at ~1,200 m altitude during the period**
 818 **highlighted in Figures 3 and 4. Calculated vertical turbulent fluxes are labeled at their respective measurement locations.**
 819 **Color scale indicates N_{3-10} particle number concentrations (cm^{-3}). The background shows a true-color satellite-corrected**
 820 **reflectance image from the overpass at 15:15 UTC, with the ocean surface appearing dark and clouds appearing white.**
 821 **Credit: NASA Worldview Snapshots.**

822 **Case 2: SPE occurring at the interface between the well-mixed surface layer and the decoupled layer**

823 **Figures 6–8 present data from June 21, 2017, with additional examples from July 7, 2017, February 18, 2018 and**
 824 **February 12, 2018, shown in Supplementary Figs. S11–S13, S14–16, and S17–S19. Back-trajectory analysis (not**
 825 **shown) indicates that the sampled air masses originated from the Arctic and were therefore expected to be relatively**
 826 **clean. Figure 6 covers approximately 4 hours of flight operations, during which the aircraft initially flew at very low**
 827 **altitudes (~30 and 50 m) near 12:00 and 13:30 UTC before gradually ascending to ~1,000 m. Drizzle number**
 828 **concentration by 2DS (purple and blue lines in Fig. 6b) was absent or below the threshold during the selected SPE**
 829 **periods. Multiple events with N_{3-10} concentrations from 10^2 to 10^4 cm^{-3} were observed throughout the second half of**
 830 **the flight. The flight trajectory (Fig. 6b) reflects predominantly east-west movement, spanning latitudes from**
 831 **approximately 38.6° to 39.3°N and longitudes from -28.4° to -27.4°W . Pink-highlighted intervals show periods with**
 832 **concurrent increases in N_3 and N_{10} concentrations exceeding 10^3 cm^{-3} , indicative occurrences of SPEs. As in Case 1,**
 833 **supermicron particle concentrations (blue in Fig. 6c) and total particle surface area (green in Fig. 6c) remained low**
 834 **during the selected SPE periods, indicating the absence of coarse-mode particles such as sea spray.**



835 **Figure 6. Same as Figure 3 but for June 21, 2017. Gaps in the time series indicate the missing data.**

837 **Figure 7a shows size-resolved particle number concentrations evolution during 13:30–14:20 UTC, encompassing the**
 838 **four pink-highlighted intervals from Fig. 6. The panel Fig. 7a displays N_{3-10} particle concentrations. High N_{3-10}**
 839 **concentrations were encountered at multiple altitudes, with maximum values exceeding $1,800 \text{ cm}^{-3}$ at ~800 m.**

Formatted: Font: 9 pt, Bold

Formatted: Space After: 12 pt, Line spacing: single

Formatted: Font: 9 pt

Deleted: Figure 5. Spatial distribution of N_{3-10} particle concentrations along the flight track during the period highlighted in Figures 3 and 4. Calculated vertical turbulent Mean calculated fluxes are labeled at their respective measurement locations on the track. Color scale indicates N_{3-10} particle number concentrations (cm^{-3}). The background shows a true-color satellite-corrected reflectance image taken from the overpass at 15:15 UTC, with the ocean surface appearing dark and clouds appearing white., Credit: NASA Worldview Snapshots.

The exact spatial location and the horizontal extent of the SPE cannot be definitely determined from aircraft measurements alone. However, substantial downward flux of N_{3-10} particles ($-41,092$ and $-2,975 \text{ cm}^{-2} \text{ s}^{-1}$) at ~1,200 m strongly suggests nucleation occurring within the entrainment zone. This interpretation is supported by the absence of N_{3-10} at ~1,600 m during 11:14–11:25 and 12:51–13:01 UTC (Fig. 3). The small particle size (3–10 nm) and less than 10 km horizontal extent argue against free tropospheric nucleation, as particles would have grown and the plume would have diluted during descent. Supplementary Figs. S8 and S9 show a downward flux of ... [2]

Formatted

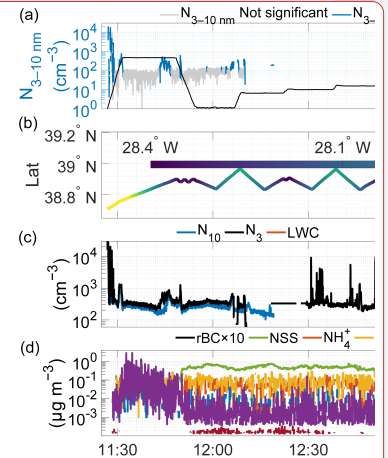
Deleted: 0

Deleted: 2... S143...165... and S176...S198

Formatted: Font color: Blue

Formatted

Deleted: Figures 6–8 present data from June 21, 2017 (with additional examples from July 7, 2017, February 18, 2018 and February 12, 2018 shown in Supplementary Figs. S10–S12, S13–15, and S16–S18). Figure 6 shows approximately 4 hours of flight ... [6]



Deleted:

Deleted:

Formatted: Caption, Space After: 12 pt

994 The potential temperature and water vapor profiles (Figs. 7b,c) show the MBL structure consisting of a well mixed
995 surface layer extending to ~ 700 m and a decoupled upper boundary layer between ~ 700 – 1300 m. Decoupled
996 structures typically form from radiative heating of the cloud layer and evaporative cooling in the sub-cloud layer,
997 which stabilize the boundary layer and suppress vertical mixing (Galewsky et al., 2022; Jones et al., 2011; Wood and
998 Bretherton, 2004). Sharp gradients in both potential temperature and mixing ratio around $1,300$ m marking the
999 entrainment zone, above which the free troposphere begins above $1,400$ m. The () profiles show higher magnitudes in
1000 the mixed layer (indicating active turbulence) and low magnitudes in both the decoupled layer (due to stratification
1001 and suppressed vertical mixing) and free troposphere. Total particle surface area remained low in the mixed layer but
1002 increased considerably toward the top of the mixed layer before decreasing in the decoupled layer and reaching very
1003 low values in the free troposphere.
1004

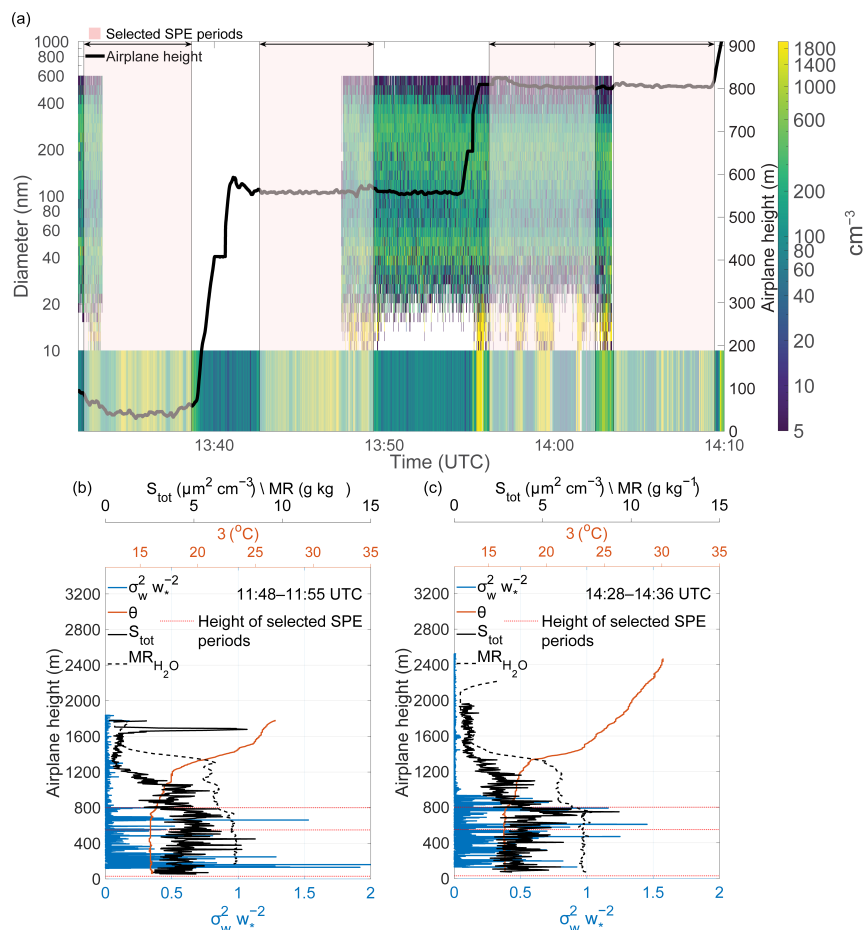


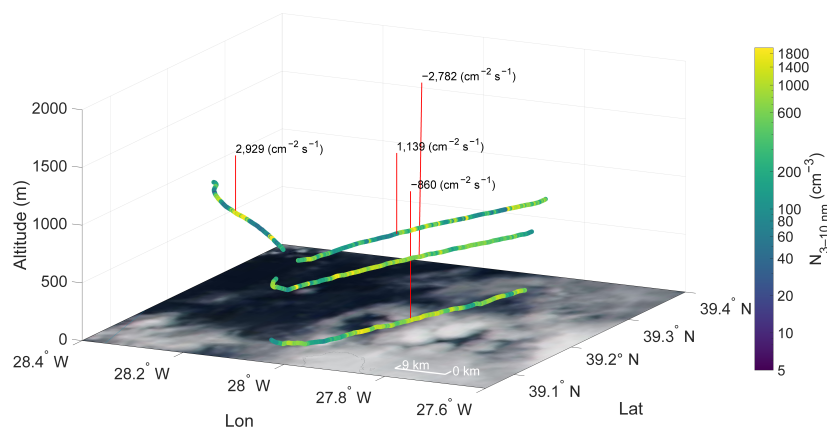
Figure 7. Same as Figure 4, but for June 21, 2017. Gaps in the time series indicate the missing data

Formatted: Font color: Blue

1005
1006
1007

1008 Figure 8 shows N_{3-10} particle concentrations along flight paths at varying altitudes: 30 m, 550 m, and two segments at
 1009 800 m. We separated the 800 m path to prevent the airplane sampling the same air mass because from 13:55–14:03
 1010 UTC the aircraft flew along the prevailing wind direction, then changed direction by 90° to fly perpendicular to the
 1011 wind. The positive vertical turbulent fluxes at 800 and negative values below suggest the SPE occurred between 550–
 1012 800 meters, likely at the top of the well mixed layer or the bottom of the decoupled layer.
 1013 The nucleation processes in the entrainment zone and at the base of the decoupled layer could be mechanistically
 1014 similar. Both locations feature the convergence of distinct air masses, in this case, the well-mixed surface layer and

1015 the stratified decoupled layer above, which generates turbulent mixing and aerosol dilution effects. While less
 1016 pronounced than at the boundary layer top, the interface between these layers exhibits comparable thermodynamic
 1017 conditions: potential temperature gradients, contrasting vapor concentrations, and localized adiabatic cooling. Figure
 1018 7 demonstrates that the decoupled layer maintains significantly lower aerosol surface area concentrations relative to
 1019 the well-mixed layer below, establishing conducive conditions for nucleation when air mass mixing occurs. A key
 1020 distinction, however, lies in the spatial characteristics, whereas entrainment zone nucleation showed limited horizontal
 1021 extent (<10 km), the decoupled layer event spanned at least 50–60 km, suggesting either more persistent favorable
 1022 conditions or a fundamentally different source mechanism operating over regional scales.



023 **Figure 8. Spatial distribution of N_{3-10} particle concentrations along the flight track at varying altitudes (30 m, 550 m, and**
 024 **800 m) during the period highlighted in Figures 6 and 7. Calculated vertical turbulent fluxes are labeled at their respective**
 025 **measurement locations. Color scale indicates N_{3-10} particle number concentrations (cm^{-3}). The background shows a true-**
 026 **color satellite reflectance image from the overpass at 14:15 UTC, with the ocean surface appearing dark and clouds**
 027 **appearing white. Credit: NASA Worldview Snapshots.**
 028

029 Figure 8 reveals a strong negative flux of N_{3-10} ($-2,782 \text{ cm}^{-2} \text{ s}^{-1}$) at 550 m that is nearly three times greater
 1030 in magnitude than the flux at 50 m ($-860 \text{ cm}^{-2} \text{ s}^{-1}$), likely due to particle evolution through growth and coagulation,
 1031 and dilution processes during vertical transport. The positive fluxes of N_{3-10} observed at 800 m ($2,929$ and $1,139 \text{ cm}^{-2}$
 1032 s^{-1}) suggest that nucleation initiated either at the top of the well-mixed boundary layer or at the bottom of the overlying
 1033 decoupled layer. This bidirectional flux structure suggests that newly formed particles were transported both upward
 1034 and downward from the formation zone through turbulent mixing. The comprehensive analysis presented in Figs. 6–
 1035 8, combined with the flux calculations in Table 1, provides some evidence that SPEs can originate within decoupled
 1036 layer structures, constituting a significant source of secondary marine aerosols in stratified boundary layer conditions.

Formatted: Normal, Space Before: 12 pt, After: 12 pt

Deleted: ¶

Deleted: Figure 8. Spatial distribution of N_{3-10} particle concentrations along the flight track at varying altitudes (30 m, 550 m, and 800 m) during the period highlighted in Figures 6 and 7. Calculated vertical turbulent fluxes are labeled at their respective measurement locations. Color scale indicates N_{3-10} particle number concentrations (cm^{-3}). The background shows a true-color satellite reflectance image from the overpass at 14:15 UTC, with the ocean surface appearing dark and clouds appearing white. Credit: NASA Worldview Snapshots. Same as Figure 3, but for June 21, 2017. The background shows a satellite-corrected reflectance image taken from the overpass at 14:15 UTC with the ocean surface appearing dark and clouds appearing white. Credit: NASA Worldview Snapshots. ¶

051 **4. Discussion**

052 This study demonstrates the value of vertical turbulent flux measurements for characterizing small particle events
053 (SPE) in remote marine boundary layers. By deriving 3–10 nm particle fluxes from aircraft measurements during the
054 ACE-ENA campaign, we identified two mechanistically distinct SPE scenarios that challenge conventional
055 understanding of marine aerosol sources. Critically, while flux sign alone identifies the vertical location of the particle
056 source, flux magnitude serves two additional essential roles: first, it must exceed the limit of detection to confirm that
057 the observed directional transport represents a statistically significant atmospheric signal rather than measurement
058 noise; and second, it provides quantitative constraints on source strength that cannot be obtained from sign alone.

059 Our analysis reveals different SPE mechanisms operating in the marine boundary layer. The first mode – entrainment
060 zone nucleation – occurs at the boundary layer top (1,200–1,400 m) where several factors create favorable conditions:
061 (1) dilution of mixed-layer air by entrained free tropospheric air causes sudden decreases in preexisting aerosol surface
062 area, (2) adiabatic cooling in rising convective plumes reduces saturation vapor pressures, and (3) turbulent
063 fluctuations in temperature and vapor concentration enhance nucleation rates (Größ et al., 2018; Nilsson et al., 2001).
064 Strong downward fluxes (up to $-41,092 \text{ cm}^{-2} \text{ s}^{-1}$) exceeding the limit of detection confirm that nucleation occurs
065 specifically within this ~200 m entrainment layer, while the absence of 3–10 nm particles above the entrainment zone
066 rules out a free tropospheric source. The limited horizontal extent (2–9 km) of these events is consistent with the
067 spatial scales of organized convective structures that develop in the upper decoupled marine boundary layer following
068 cold front passages in the Azores region, where cumulus-associated drizzle reduces the condensation sink to levels
069 favorable for nucleation (Etling and Brown, 1993; Zheng et al., 2021).

070 The large difference in flux magnitudes between the two entrainment zone events ($-41,092$ vs. $-2,975 \text{ cm}^{-2} \text{ s}^{-1}$)
071 provides information that flux sign alone cannot supply: it reflects spatial heterogeneity in source strength and the
072 proximity of the aircraft to the nucleation zone during each transect. These flux magnitudes, integrated over the
073 duration of the events, represent a substantial source of freshly nucleated particles to the marine aerosol number
074 budget, constraints that can be used directly to evaluate nucleation parameterizations in regional and global models.
075 While the ultimate contribution of these particles to CCN populations depends on growth timescales and loss processes
076 during vertical transport (requiring ~24–48 hours at typical marine growth rates of $\sim 1 \text{ nm hr}^{-1}$ to reach CCN-relevant
077 sizes; (Zheng et al., 2021)), the flux-based constraints provided here represent a necessary observational foundation
078 for quantifying this contribution in future studies. Our analysis reveals a second distinct mode of SPE occurring within

079 decoupled marine boundary layer structures, where particles originate at the interface between the well-mixed surface
080 layer and the overlying decoupled layer (~700–800 m altitude). While mechanistically similar to entrainment zone
081 processes through air mass convergence, thermodynamic gradients, and aerosol dilution effects, decoupled layer
082 nucleation occurs within the boundary layer structure rather than at its top, operating under conditions of reduced
083 aerosol surface area concentrations and stratified vertical mixing. This mode exhibits a regional-scale horizontal extent
084 (>50 km) compared to the localized nature (<10 km) of entrainment zone events. The substantial negative flux
085 magnitudes observed at intermediate altitudes ($-2,782 \text{ cm}^{-2} \text{ s}^{-1}$ at 550 m) combined with positive fluxes aloft
086 demonstrate active particle redistribution throughout the marine boundary layer. The factor of ~3 difference in flux

Deleted: ¶

Deleted: ¶

Formatted: Font color: Blue

Deleted: new particle formation (NPF)

Deleted: NPF

Formatted: Font color: Blue

Deleted: NPF

Formatted: Font color: Blue

Deleted: and

Deleted: provide direct evidence that nucleation occurs specifically in this ~200 m layer

Deleted: The limited horizontal extent (2–9 km) of these events

Deleted: , comparable to the wavelength-to-depth ratios of convective roll vortices (Etling and Brown, 1993; Hartmann et al., 1997), suggests that organized boundary layer convection may concentrate precursor vapors and newly formed particles into coherent structures.¶

Deleted: new particle formation

Formatted: Font color: Blue

1102 magnitude between the 550 m and 30 m levels ($-2,782$ vs. -860 $\text{cm}^{-2} \text{s}^{-1}$) is consistent with attenuation of the particle
1103 flux during downward transport through dilution with ambient air, as well as losses through coagulation and growth
1104 out of the 3–10 nm size range. This vertical divergence in flux magnitude represents a quantitative signature of particle
1105 evolution during transport that flux sign alone would be incapable of revealing. This mode represents a significant and
1106 previously underappreciated source of secondary marine aerosols that can efficiently contribute to regional aerosol
1107 budgets through direct incorporation into the surface mixed layer where particles undergo growth to cloud-relevant
1108 sizes.

Deleted: , suggesting t

Deleted: cloud condensation nuclei

Formatted: Font color: Blue

1109 5. Conclusions

1110 The occurrence of newly formed particles in marine environments has been documented in a number of previous
1111 studies. Wiedensohler et al., (1996) observed sub-20 nm particles originating from the free troposphere or cloud tops
1112 within the MBL and mixed downwards over the open ocean, suggesting in-situ production based on correlations with
1113 absolute humidity. Covert et al., (1992) reported sub-20 nm particle production near precipitating cloud tops within
1114 the MBL, where larger particles acting as condensation sinks had been scavenged by precipitation, with sub-20 nm
1115 particles dominating 10% of the campaign and indicating episodic rather than continuous production. O'Dowd et al.,
1116 (2002) documented NPF events at the coastal Mace Head station when marine air masses encountered biogenic
1117 emissions from the intertidal zone. The ACORES campaign, conducted over the Azores at the same time as ACE-
1118 ENA, reported freshly nucleated particle bursts near the cloud top exceeding background MBL concentrations by
1119 more than an order of magnitude (Siebert et al., 2021). Concurrent helicopter-borne particle flux measurements over
1120 the Azores during ACORES (Lückerath et al., 2022) also documented particle fluxes in the marine boundary layer,
1121 providing complementary observational context to our aircraft-based approach. The prevailing theoretical framework,
1122 based on relatively high sea spray aerosol surface area acting as condensation and coagulation sinks (Bates et al.,
1123 1998; Pirjola et al., 2000), nonetheless predicted that NPF should rarely occur in remote marine boundary layers over
1124 open oceans. Our flux-based observations build on this existing framework by providing the first direct constraints on
1125 the vertical source location and strength of freshly nucleated particles in the remote marine boundary layer. Low
1126 aerosol surface area and specific meteorological configurations can create localized or regional zones where conditions
1127 become favorable. For entrainment zone and decoupled layer events, extremely low aerosol concentrations, combined
1128 with turbulent mixing and adiabatic cooling can create a transient "window" where nucleation can proceed despite
1129 moderate surface area concentrations lower in the boundary layer. Recent ground-based observations from the same
1130 campaign (Zheng et al., 2021) documented frequent NPF events but could not definitively determine vertical location.
1131 Our flux-based approach resolves this ambiguity by providing direct evidence of where particles originate relative to
1132 the measurement location. The negative (downward) fluxes in Case 1 unambiguously demonstrate an above-aircraft
1133 source, while the bidirectional fluxes in Case 2 indicate a distributed source encompassing the measurement altitude.
1134 These findings have important implications for understanding marine aerosol budgets. The spatial scales of these two
1135 SPE modes differ by an order of magnitude: entrainment zone events exhibited limited horizontal extents (<10 km),
1136 consistent with localized convective structures, while decoupled layer events spanned regional scales (50–60 km),
1137 suggesting fundamentally different formation mechanisms or persistence of favorable conditions. For the entrainment

Deleted: (

Deleted: (

Deleted: (

Deleted: The prevailing theoretical framework, based on relatively high sea spray aerosol surface area acting as condensation and coagulation sinks (Bates et al., 1998; Pirjola et al., 2000), predicted that NPF should rarely occur in remote marine boundary layers over open oceans. Our observations demonstrate that this framework is incomplete.

Deleted: CCN

Deleted: Notably,

Deleted: t

Deleted: NPF

153 zone mode, while the aircraft sampled the SPE for only ~4 minutes during each transect due to its high ground speed,
154 NPF events in marine and continental environments are typically observed to persist for 2–5 hours (Kulmala et al.,
155 2004; Zheng et al., 2021; Islam et al., 2022). Assuming the measured downward flux of $-41,092 \text{ cm}^{-2} \text{ s}^{-1}$ is
156 representative of a nucleation event of typical duration of ~3 hours and using a mixed layer depth of ~1,200 m, the
157 estimated increase in vertically integrated particle number concentration is approximately:

$$\Delta N_{3-10} \approx |F| \times \frac{\Delta t}{z_{MBL}} = \frac{41,092 \times 10,800}{1.2 \times 10^5} \approx 3,700 \text{ cm}^{-3}$$

159 where F is the flux in $\text{cm}^{-2} \text{ s}^{-1}$, Δt is the event duration in seconds, and z_{MBL} is the mixed layer depth in cm. This
160 represents a substantial addition to the total particle number concentration in the surface mixed layer, noting that this
161 estimate refers to freshly nucleated 3–10 nm particles rather than CCN-relevant particles. The fraction surviving to
162 CCN-relevant sizes ($>50\text{--}80 \text{ nm}$) depends on growth rates and loss processes that cannot be quantified from single
163 aircraft transects alone. However, Zheng et al. (2021) estimated that under favorable conditions at the same site, newly
164 formed particles contributed on average ~50% of total CCN concentrations following cold front passages, suggesting
165 that even accounting for coagulation losses, the contribution of entrainment zone nucleation to the marine CCN budget
166 may be substantial. Entrainment zone nucleation, despite its limited horizontal extent, may contribute significantly to
167 the marine aerosol number budget through sustained downward transport via convective mixing. Though flux
168 magnitudes for the decoupled layer nucleation events ($-2,782 \text{ cm}^{-2} \text{ s}^{-1}$) are less pronounced, their large spatial extent
169 likely results in comparable or larger aggregate contributions to regional aerosol budgets. We note that the contribution
170 of freshly nucleated particles to CCN population depends on growth rates and loss processes during transport and
171 cannot be assessed from short-term measurements alone. The flux magnitudes and vertical source locations reported
172 here provide the observational foundation needed to evaluate this contribution quantitatively in future studies
173 combining particle flux measurements with growth rate and CCN closure analyses.

174 Our observations, combined with combined with the longer history of marine NPF observations cited above and recent
175 ground-based measurements from the same campaign (Zheng et al., 2021), suggest that the contribution of in-situ
176 marine boundary layer nucleation to the aerosol budget may be more significant than current model representations
177 assume. Climate models have historically followed theoretical expectations that marine boundary layer nucleation
178 should be negligible, instead representing new particles as primarily originating from free tropospheric entrainment
179 or long-range continental transport (Clarke et al., 2013; Logan et al., 2014), with marine boundary layer nucleation
180 treated as negligible. The frequent occurrence of SPE during the ACE-ENA campaign (entrainment zone nucleation
181 in 2 and decoupled layer nucleation in 4 of 39 flights analyzed) suggests that marine boundary layer nucleation – in
182 both modes – may be more climatologically important than previously recognized. Given that marine boundary layer
183 cloud microphysical properties exhibit the highest sensitivity to aerosol changes (Bellouin et al., 2020; Zhang et al.,
184 2024), and that even modest changes in CCN concentrations can substantially affect cloud radiative forcing in these
185 pristine environments, proper representation of NPF sources is critical for reducing uncertainties in aerosol-cloud
186 interaction estimates.

187 The continuous wavelet transform (CWT) approach proved essential for deriving reliable fluxes from fast-moving
188 aircraft platforms. Traditional eddy covariance methods require stationarity conditions that are difficult to maintain
189 during aircraft sampling, where the platform continuously moves through different air masses. The CWT method's

Deleted: Entrainment zone nucleation, despite limited horizontal extent, may contribute significantly to CCN populations through sustained downward transport via convective mixing. The calculated flux of $-41,092 \text{ cm}^{-2} \text{ s}^{-1}$ integrated over several hours could deliver substantial numbers of particles to the surface mixed layer where they can grow to CCN sizes. Though flux magnitudes for the decoupled layer nucleation events ($-2,782 \text{ cm}^{-2} \text{ s}^{-1}$) are less pronounced, their large spatial extent likely makes even larger contributions to regional CCN budgets.

Moved (insertion) [2]

Deleted: demonstrate that this representation misses an important aerosol source.

Moved up [2]: Climate models have historically followed theoretical expectations that marine boundary layer nucleation should be negligible, instead representing new particles as primarily originating from free tropospheric entrainment or long-range continental transport (Clarke et al., 2013; Logan et al., 2014)

Deleted: .

Deleted: NPF events

1208 ability to handle non-stationary data while avoiding systematic errors from linear detrending (Rannik and Vesala,
1209 1999; Schaller et al., 2017) enabled flux calculations even during complex meteorological conditions. Our detailed
1210 analysis of frequency response and flux loss corrections demonstrates that 1 Hz CPC measurements, while not ideal,
1211 can resolve sufficient turbulent scales to capture the dominant flux contributions when proper corrections are applied.
1212 *Importantly, flux magnitudes (not just flux sign) provide essential scientific value: they must exceed the limit of*
1213 *detection to confirm statistical significance, they constrain source strength and proximity, and they provide*
1214 *quantitative inputs for evaluating nucleation parameterizations in regional and global models.* As the scientific
1215 community works to reduce uncertainties in aerosol-cloud interactions, flux-based approaches offer a promising path
1216 forward for understanding how, where, and when new particles form in Earth's remote marine atmosphere.
1217 Several limitations warrant acknowledgment. First, our 3–10 nm size range likely misses the initial nucleation at
1218 molecular cluster sizes (~1–3 nm), meaning we observe "small particle events" rather than nucleation itself. However,
1219 the rapid appearance of 3–10 nm particles with clear vertical structure in turbulent fluxes provides strong indirect
1220 evidence for nearby nucleation. Second, the aircraft's high ground speed (~100 m s⁻¹) compared to typical tower-based
1221 measurements introduces challenges for capturing the full turbulent spectrum, particularly at lower altitudes where
1222 eddy sizes are smaller. Our flux loss corrections (F_m/F ratios of 0.70–0.99) account for this limitation but introduce
1223 additional uncertainty. Third, we cannot determine definitively the exact horizontal extent of NPF events from single
1224 aircraft transects, though crosswind sampling provides minimum extent estimates.

Formatted: Font: Italic

1225 **Future Directions**

1226 This work establishes aircraft-derived aerosol fluxes as a valuable tool for characterizing marine boundary layer
1227 aerosol sources. Several directions would advance understanding:

1228 **Slower aircrafts:** Unmanned aerial vehicles operating at 30–40 m s⁻¹ would better resolve small-scale turbulence,
1229 particularly near the surface, where flux loss corrections are currently largest, improving flux accuracy and enabling
1230 more detailed vertical structure analysis.

1231 **Expanded measurements:** Simultaneous flux measurements of precursor gases (H₂SO₄, NH₃, amines, organics)
1232 would directly test hypotheses about nucleation mechanisms and identify which chemical pathways dominate in
1233 different scenarios.

1234 **Multi-aircraft coordination:** Coordinated measurements from more than one aircraft at different altitudes could
1235 directly observe vertical particle transport rates and evolution, constraining growth rates and loss processes during
1236 transit.

1237 **Longer-term statistics:** Expanding beyond campaign-based measurements to seasonal or annual timescales would
1238 quantify the climatological importance of different NPF modes and their relationships to synoptic meteorological
1239 patterns.

1240 **Model evaluation:** Using observed flux *magnitudes and vertical source locations* as benchmarks for evaluating marine
1241 boundary layer nucleation parameterizations in regional and global models would improve their representation of
1242 aerosol-cloud interactions *and reduce uncertainties in aerosol indirect forcing estimates.*

Deleted: es

Deleted: .

1245 **Code availability**

1246 All the scripts used to make the figures used in this study will be available along with the supplementary information

1247 **Data availability**

1248 All data from the ACE-ENA campaign are archived at the DOE ARM data center, covering measurements from the
1249 ARM Aerial Facility near ARM ENA site on Graciosa Island (June 15, 2017 - February 28, 2018).

1250 ARM Aerial Facility (AAF) Merged VAP, <https://doi.org/10.5439/1999133>, (AAFMERGED, (Mei and Gaustad,
1251 2024)

1252 ARM Aerial Facility (AAF) Merged aerosol size distribution, <https://doi.org/10.5439/1905541>,
1253 (AAFMERGEDAEROSOLS,(Pekour and Ermold, 2017)

1254 ARM Aerial Facility Isokinetic Inlet, <https://doi.org/10.5439/1241544>, (AAFINLETISOK, (Koontz et al., 2016)

1255 ARM Aerial Facility (AAF) Aircraft Integrated Meteorological Measurement System (AIMMS) - Meteorological
1256 data, <https://doi.org/10.5439/1349241>, (AAFMETAIMS,(Matthews and Goldberger, 2020)

1257 Interagency Working Group for Airborne Data and Telemetry Systems,
1258 <https://adc.arm.gov/discovery/#/results/s::aaf%20iwg/iopShortName::aaf2017ace-ena>, (IWG ACEENA)

1259 Proton Transfer Reaction Mass Spectrometer (PTR-MS),
1260 https://adc.arm.gov/discovery/#/results/instrument_code::ptrms/iopShortName::aaf2017ace-ena, (ACE ENA IOPI
1261 G1 PTRMS)

1262 **Author contribution**

1263 ARS, MDP, and NM conceptualized the study. ARS performed the data curation, formal analysis, and designed the
1264 figures with contributions from MDP and NM. NM acquired the financial support for the project. ARS and NM wrote
1265 the paper, and all authors provided input on the paper for revision before submission.

1266 **Competing interests**

1267 The authors declare that they have no conflict of interest.

1268 **Acknowledgements**

1269 We acknowledge the Atmospheric Radiation Measurement (ARM) Climate Research Facility, a user facility of the
1270 United States Department of Energy (US DOE), Office of Science, sponsored by the Office of Biological and
1271 Environmental Research. We thank Dr. Jian Wang and all the staff responsible for the operation of the ACE-ENA
1272 campaign. We acknowledge the use of imagery from the NASA Worldview application, part of the NASA Earth
1273 Observing System Data and Information System (EOSDIS). AI tools were used to correct the spelling and sentence
1274 structure of the manuscript

1275 **Financial support**

1276 This work was supported by the DOE Office of Science, Biological and Environment Research, Grant No. DE-
1277 SC0024873

1278 **References**

- 1279 Andreae, M. O.: Aerosols Before Pollution, *Science*, 315, 50–51, <https://doi.org/10.1126/science.1136529>, 2007.
- 1280 Aubinet, M., Vesala, T., and Papale, D. (Eds.): *Eddy Covariance: A Practical Guide to Measurement and Data*
1281 *Analysis*, Springer Netherlands, Dordrecht, <https://doi.org/10.1007/978-94-007-2351-1>, 2012.
- 1282 Bates, T. S., Kapustin, V. N., Quinn, P. K., Covert, D. S., Coffman, D. J., Mari, C., Durkee, P. A., De Bruyn, W. J.,
1283 and Saltzman, E. S.: Processes controlling the distribution of aerosol particles in the lower marine boundary layer
1284 during the First Aerosol Characterization Experiment (ACE 1), *J. Geophys. Res. Atmospheres*, 103, 16369–16383,
1285 <https://doi.org/10.1029/97JD03720>, 1998.
- 1286 Bellouin, N., Quaas, J., Gryspeerdt, E., Kinne, S., Stier, P., Watson-Parris, D., Boucher, O., Carslaw, K. S.,
1287 Christensen, M., Daniiau, A. -L., Dufresne, J. -L., Feingold, G., Fiedler, S., Forster, P., Gettelman, A., Haywood, J.
1288 M., Lohmann, U., Malavelle, F., Mauritsen, T., McCoy, D. T., Myhre, G., Müllmenstädt, J., Neubauer, D., Possner,
1289 A., Rugenstein, M., Sato, Y., Schulz, M., Schwartz, S. E., Sourdeval, O., Storelvmo, T., Toll, V., Winker, D., and
1290 Stevens, B.: Bounding Global Aerosol Radiative Forcing of Climate Change, *Rev. Geophys.*, 58, e2019RG000660,
1291 <https://doi.org/10.1029/2019RG000660>, 2020.
- 1292 Boers, R. and Eloranta, E. W.: Lidar measurements of the atmospheric entrainment zone and the potential temperature
1293 jump across the top of the mixed layer, *Bound.-Layer Meteorol.*, 34, 357–375, <https://doi.org/10.1007/BF00120988>,
1294 1986.
- 1295 Carslaw, K. S., Lee, L. A., Reddington, C. L., Pringle, K. J., Rap, A., Forster, P. M., Mann, G. W., Spracklen, D. V.,
1296 Woodhouse, M. T., Regayre, L. A., and Pierce, J. R.: Large contribution of natural aerosols to uncertainty in indirect
1297 forcing, *Nature*, 503, 67–71, <https://doi.org/10.1038/nature12674>, 2013.
- 1298 Clarke, A. D., Freitag, S., Simpson, R. M. C., Hudson, J. G., Howell, S. G., Brekhovskikh, V. L., Campos, T.,
1299 Kapustin, V. N., and Zhou, J.: Free troposphere as a major source of CCN for the equatorial pacific boundary layer:
1300 long-range transport and teleconnections, *Atmospheric Chem. Phys.*, 13, 7511–7529, <https://doi.org/10.5194/acp-13-7511-2013>, 2013.
- 1302 Covert, D. S., Kapustin, V. N., Quinn, P. K., and Bates, T. S.: New particle formation in the marine boundary layer,
1303 *J. Geophys. Res. Atmospheres*, 97, 20581–20589, <https://doi.org/10.1029/92JD02074>, 1992.
- 1304 Dal Maso, M., Kulmala, M., Riipinen, I., Wagner, R., Hussein, T., Aalto, P. P., and Lehtinen, K.: Formation and
1305 growth of fresh atmospheric aerosols: eight years of aerosol size distribution data from SMEAR II, Hyytiälä, Finland,
1306 *Boreal Environ. Res.*, 10, 323–336, 2005.
- 1307 Deardorff, J. W.: Three-dimensional numerical study of turbulence in an entraining mixed layer, *Bound.-Layer*
1308 *Meteorol.*, 7, 199–226, <https://doi.org/10.1007/BF00227913>, 1974.
- 1309 Desjardins, R. L., MacPherson, J. I., Schuepp, P. H., and Karanja, F.: An evaluation of aircraft flux measurements of
1310 CO₂, water vapor and sensible heat, *Bound.-Layer Meteorol.*, 47, 55–69, 1989.
- 1311 Dewani, N., Sakradzija, M., Schlemmer, L., Leinweber, R., and Schmidli, J.: Dependency of vertical velocity variance
1312 on meteorological conditions in the convective boundary layer, *Atmospheric Chem. Phys.*, 23, 4045–4058,
1313 <https://doi.org/10.5194/acp-23-4045-2023>, 2023.

- 1314 Ehn, M., Vuollekoski, H., Petäjä, T., Kerminen, V., Vana, M., Aalto, P., de Leeuw, G., Ceburnis, D., Dupuy, R.,
 1315 O'Dowd, C. D., and Kulmala, M.: Growth rates during coastal and marine new particle formation in western Ireland,
 1316 *J. Geophys. Res. Atmospheres*, 115, 2010JD014292, <https://doi.org/10.1029/2010JD014292>, 2010.
- 1317 Fan, M. and Pekour, M.: CPC_ACEENA, <https://doi.org/10.5439/1440985>, 2018.
- 1318 Foken, T., Wimmer, F., Mauder, M., Thomas, C., and Liebethal, C.: Some aspects of the energy balance closure
 1319 problem, *Atmospheric Chem. Phys.*, 6, 4395–4402, <https://doi.org/10.5194/acp-6-4395-2006>, 2006.
- 1320 Galewsky, J., Jensen, M. P., and Delp, J.: Marine Boundary Layer Decoupling and the Stable Isotopic Composition
 1321 of Water Vapor, *J. Geophys. Res. Atmospheres*, 127, e2021JD035470, <https://doi.org/10.1029/2021JD035470>, 2022.
- 1322 Gioli, B., Miglietta, F., De Martino, B., Hutjes, R. W. A., Dolman, H. A. J., Lindroth, A., Schumacher, M., Sanz, M.
 1323 J., Manca, G., Peressotti, A., and Dumas, E. J.: Comparison between tower and aircraft-based eddy covariance fluxes
 1324 in five European regions, *Agric. For. Meteorol.*, 127, 1–16, <https://doi.org/10.1016/j.agrformet.2004.08.004>, 2004.
- 1325 Größ, J., Hamed, A., Sonntag, A., Spindler, G., Elina Manninen, H., Nieminen, T., Kulmala, M., Hörrak, U., Plass-
 1326 Dülmer, C., Wiedensohler, A., and Birmili, W.: Atmospheric new particle formation at the research station Melpitz,
 1327 Germany: connection with gaseous precursors and meteorological parameters, *Atmospheric Chem. Phys.*, 18, 1835–
 1328 1861, <https://doi.org/10.5194/acp-18-1835-2018>, 2018.
- 1329 Helbig, M., Gerken, T., Beamesderfer, E. R., Baldochi, D. D., Banerjee, T., Biraud, S. C., Brown, W. O. J., Brunzell,
 1330 N. A., Burakowski, E. A., Burns, S. P., Butterworth, B. J., Chan, W. S., Davis, K. J., Desai, A. R., Fuentes, J. D.,
 1331 Hollinger, D. Y., Kljun, N., Mauder, M., Novick, K. A., Perkins, J. M., Rahn, D. A., Rey-Sanchez, C., Santanello, J.
 1332 A., Scott, R. L., Seyednasrollah, B., Stoy, P. C., Sullivan, R. C., de Arellano, J. V.-G., Wharton, S., Yi, C., and
 1333 Richardson, A. D.: Integrating continuous atmospheric boundary layer and tower-based flux measurements to advance
 1334 understanding of land-atmosphere interactions, *Agric. For. Meteorol.*, 307, 108509,
 1335 <https://doi.org/10.1016/j.agrformet.2021.108509>, 2021.
- 1336 Hoose, C., Kristjánsson, J. E., Iversen, T., Kirkevåg, A., Seland, Ø., and Gettelman, A.: Constraining cloud droplet
 1337 number concentration in GCMs suppresses the aerosol indirect effect, *Geophys. Res. Lett.*, 36, 2009GL038568,
 1338 <https://doi.org/10.1029/2009GL038568>, 2009.
- 1339 Horst, T. W.: A Simple Formula for Attenuation of Eddy Fluxes Measured with First-Order Scalar Sensors, *Bound.-*
 1340 *Layer Meteorol.*, 82, 219–233, <https://doi.org/10.1023/A:1000229130034>, 1997.
- 1341 Intergovernmental Panel on Climate Change (IPCC): Climate Change 2021 – The Physical Science Basis: Working
 1342 Group I Contribution to the Sixth Assessment Report of the Intergovernmental Panel on Climate Change, 1st ed.,
 1343 Cambridge University Press, <https://doi.org/10.1017/9781009157896>, 2023.
- 1344 Islam, M. M., Meskhidze, N., Rasheeda Sathesh, A., and Petters, M. D.: Turbulent Flux Measurements of the Near-
 1345 Surface and Residual-Layer Small Particle Events, *J. Geophys. Res. Atmospheres*, 127, e2021JD036289,
 1346 <https://doi.org/10.1029/2021JD036289>, 2022.
- 1347 Jones, C. R., Bretherton, C. S., and Leon, D.: Coupled vs. decoupled boundary layers in VOCALS-REx, *Atmospheric*
 1348 *Chem. Phys.*, 11, 7143–7153, <https://doi.org/10.5194/acp-11-7143-2011>, 2011.
- 1349 Kaimal, J. C. and Finnigan, J. J.: *Atmospheric Boundary Layer Flows: Their Structure and Measurement*, Oxford
 1350 University Press, <https://doi.org/10.1093/oso/9780195062397.001.0001>, 1994.
- 1351 Koontz, A., Mei, F., and Pekour, M.: aafinletisok.a1, <https://doi.org/10.5439/1241544>, 2016.
- 1352 Korolev, A. and Isaac, G. A.: Shattering during Sampling by OAPs and HVPS. Part I: Snow Particles, *J. Atmospheric*
 1353 *Ocean. Technol.*, 22, 528–542, <https://doi.org/10.1175/JTECH1720.1>, 2005.

1354 Kuang, C. and Mei, F.: Condensation Particle Counter (CPC) Instrument Handbook - Airborne Version,
1355 <https://doi.org/10.2172/1562676>, 2019.

1356 Kulkarni, P. and Wang, J.: New fast integrated mobility spectrometer for real-time measurement of aerosol size
1357 distribution: II. Design, calibration, and performance characterization, *J. Aerosol Sci.*, 37, 1326–1339,
1358 <https://doi.org/10.1016/j.jaerosci.2006.01.010>, 2006a.

1359 Kulkarni, P. and Wang, J.: New fast integrated mobility spectrometer for real-time measurement of aerosol size
1360 distribution—I: Concept and theory, *J. Aerosol Sci.*, 37, 1303–1325, <https://doi.org/10.1016/j.jaerosci.2006.01.005>,
1361 2006b.

1362 Kulmala, M., Petäjä, T., Nieminen, T., Sipilä, M., Manninen, H. E., Lehtipalo, K., Dal Maso, M., Aalto, P. P.,
1363 Junninen, H., Paasonen, P., Riipinen, I., Lehtinen, K. E. J., Laaksonen, A., and Kerminen, V.-M.: Measurement of the
1364 nucleation of atmospheric aerosol particles, *Nat. Protoc.*, 7, 1651–1667, <https://doi.org/10.1038/nprot.2012.091>, 2012.

1365 Lee, X., Massman, W., and Law, B. (Eds.): *Handbook of Micrometeorology: A Guide for Surface Flux Measurement
1366 and Analysis*, Springer Netherlands, Dordrecht, 250 pp., <https://doi.org/10.1007/1-4020-2265-4>, 2005.

1367 Lenschow, D. H. and Stankov, B. B.: Length Scales in the Convective Boundary Layer, *J. Atmospheric Sci.*, 43, 1198–
1368 1209, [https://doi.org/10.1175/1520-0469\(1986\)043<1198:LSITCB>2.0.CO;2](https://doi.org/10.1175/1520-0469(1986)043<1198:LSITCB>2.0.CO;2), 1986.

1369 Lenschow, D. H., Wulfmeyer, V., and Senff, C.: Measuring Second- through Fourth-Order Moments in Noisy Data,
1370 *J. Atmospheric Ocean. Technol.*, 17, 1330–1347, [https://doi.org/10.1175/1520-0426\(2000\)017<1330:MSTFOM>2.0.CO;2](https://doi.org/10.1175/1520-0426(2000)017<1330:MSTFOM>2.0.CO;2), 2000.

1372 Li, Y., Wu, Y., Tang, J., Zhu, P., Gao, Z., and Yang, Y.: Quantitative Evaluation of Wavelet Analysis Method for
1373 Turbulent Flux Calculation of Non-Stationary Series, *Geophys. Res. Lett.*, 50, e2022GL101591,
1374 <https://doi.org/10.1029/2022GL101591>, 2023.

1375 Logan, T., Xi, B., and Dong, X.: Aerosol properties and their influences on marine boundary layer cloud condensation
1376 nuclei at the ARM mobile facility over the Azores, *J. Geophys. Res. Atmospheres*, 119, 4859–4872,
1377 <https://doi.org/10.1002/2013JD021288>, 2014.

1378 Lücknerath, J., Held, A., Siebert, H., Michalkow, M., and Wehner, B.: Vertical aerosol particle exchange in the marine
1379 boundary layer estimated from helicopter-borne measurements in the Azores region, *Atmospheric Chem. Phys.*, 22,
1380 10007–10021, <https://doi.org/10.5194/acp-22-10007-2022>, 2022.

1381 Martin, S., Beyrich, F., and Bange, J.: Observing Entrainment Processes Using a Small Unmanned Aerial Vehicle: A
1382 Feasibility Study, *Bound.-Layer Meteorol.*, 150, 449–467, <https://doi.org/10.1007/s10546-013-9880-4>, 2014.

1383 Mather, J. H. and Voyles, J. W.: The Arm Climate Research Facility: A Review of Structure and Capabilities, *Bull.
1384 Am. Meteorol. Soc.*, 94, 377–392, <https://doi.org/10.1175/BAMS-D-11-00218.1>, 2013.

1385 Matthews, A. and Goldberger, L.: *Aircraft-Integrated Meteorological Measurement System (AIMMS) Instrument
1386 Handbook*, <https://doi.org/10.2172/1725866>, 2020.

1387 Mei, F. and Gaustad, K.: ARM Aerial Facility (AAF) Merged Value-Added Product Report for Historical G-1 Field
1388 Campaigns, Oak Ridge National Laboratory (ORNL), Oak Ridge, TN (United States). Atmospheric Radiation
1389 Measurement (ARM) Data Center, <https://doi.org/10.2172/2335708>, 2024.

1390 Meskhidze, N., Xu, J., Gantt, B., Zhang, Y., Nenes, A., Ghan, S. J., Liu, X., Easter, R., and Zaveri, R.: Global
1391 distribution and climate forcing of marine organic aerosol: 1. Model improvements and evaluation, *Atmospheric
1392 Chem. Phys.*, 11, 11689–11705, <https://doi.org/10.5194/acp-11-11689-2011>, 2011.

1393 Meskhidze, N., Jaimes-Correa, J. C., Petters, M. D., Royalty, T. M., Phillips, B. N., Zimmerman, A., and Reed, R.:
1394 Possible Wintertime Sources of Fine Particles in an Urban Environment, *J. Geophys. Res. Atmospheres*, 124, 13,055-
1395 13,070, <https://doi.org/10.1029/2019JD031367>, 2019.

1396 Misztal, P. K., Karl, T., Weber, R., Jonsson, H. H., Guenther, A. B., and Goldstein, A. H.: Airborne flux measurements
1397 of biogenic isoprene over California, *Atmospheric Chem. Phys.*, 14, 10631–10647, <https://doi.org/10.5194/acp-14-10631-2014>, 2014.

1399 Modini, R. L., Ristovski, Z. D., Johnson, G. R., He, C., Surawski, N., Morawska, L., Suni, T., and Kulmala, M.: New
1400 particle formation and growth at a remote, sub-tropical coastal location, *Atmospheric Chem. Phys.*, 9, 7607–7621,
1401 <https://doi.org/10.5194/acp-9-7607-2009>, 2009.

1402 Nieminen, T., Kerminen, V.-M., Petäjä, T., Aalto, P. P., Arshinov, M., Asmi, E., Baltensperger, U., Beddows, D. C.
1403 S., Beukes, J. P., Collins, D., Ding, A., Harrison, R. M., Henzing, B., Hooda, R., Hu, M., Hörrak, U., Kivekäs, N.,
1404 Komsaare, K., Krejci, R., Kristensson, A., Laakso, L., Laaksonen, A., Leaitch, W. R., Lihavainen, H., Mihalopoulos,
1405 N., Németh, Z., Nie, W., O’Dowd, C., Salma, I., Sellegri, K., Svenningsson, B., Swietlicki, E., Tunved, P., Ulevicius,
1406 V., Vakkari, V., Vana, M., Wiedensohler, A., Wu, Z., Virtanen, A., and Kulmala, M.: Global analysis of continental
1407 boundary layer new particle formation based on long-term measurements, *Atmospheric Chem. Phys.*, 18, 14737–
1408 14756, <https://doi.org/10.5194/acp-18-14737-2018>, 2018.

1409 Nilsson, E. D., Rannik, Ü., Kulmala, M., Buzorius, G., and O’Dowd, C. D.: Effects of continental boundary layer
1410 evolution, convection, turbulence and entrainment, on aerosol formation, *Tellus Ser. B Chem. Phys. Meteorol. B*, 53,
1411 441–461, <https://doi.org/10.3402/tellusb.v53i4.16617>, 2001.

1412 Novak, G. A., Fite, C. H., Holmes, C. D., Veres, P. R., Neuman, J. A., Faloona, I., Thornton, J. A., Wolfe, G. M.,
1413 Vermeuel, M. P., Jernigan, C. M., Peischl, J., Ryerson, T. B., Thompson, C. R., Bourgeois, I., Warneke, C., Gkatzelis,
1414 G. I., Coggon, M. M., Sekimoto, K., Bui, T. P., Dean-Day, J., Diskin, G. S., DiGangi, J. P., Nowak, J. B., Moore, R.
1415 H., Wiggins, E. B., Winstead, E. L., Robinson, C., Thornhill, K. L., Sanchez, K. J., Hall, S. R., Ullmann, K., Dollner,
1416 M., Weinzierl, B., Blake, D. R., and Bertram, T. H.: Rapid cloud removal of dimethyl sulfide oxidation products limits
1417 SO₂ and cloud condensation nuclei production in the marine atmosphere, *Proc. Natl. Acad. Sci.*, 118, e2110472118,
1418 <https://doi.org/10.1073/pnas.2110472118>, 2021.

1419 O’Dowd, C., Monahan, C., and Dall’Osto, M.: On the occurrence of open ocean particle production and growth events,
1420 *Geophys. Res. Lett.*, 37, 2010GL044679, <https://doi.org/10.1029/2010GL044679>, 2010.

1421 O’Dowd, C. D., Hämeri, K., Mäkelä, J., Väkeva, M., Aalto, P., de Leeuw, G., Kunz, G. J., Becker, E., Hansson, H.,
1422 Allen, A. G., Harrison, R. M., Berresheim, H., Kleefeld, C., Geever, M., Jennings, S. G., and Kulmala, M.: Coastal
1423 new particle formation: Environmental conditions and aerosol physicochemical characteristics during nucleation
1424 bursts, *J. Geophys. Res. Atmospheres*, 107, <https://doi.org/10.1029/2000JD000206>, 2002.

1425 Olfert, J. S., Kulkarni, P., and Wang, J.: Measuring aerosol size distributions with the fast integrated mobility
1426 spectrometer, *J. Aerosol Sci.*, 39, 940–956, <https://doi.org/10.1016/j.jaerosci.2008.06.005>, 2008.

1427 Pekour, M. and Ermold, B.: ARM Aerial Facility (AAF) Merged aerosol size distribution,
1428 <https://doi.org/10.5439/1905541>, 2017.

1429 Petters, M. D., Snider, J. R., Stevens, B., Vali, G., Faloona, I., and Russell, L. M.: Accumulation mode aerosol, pockets
1430 of open cells, and particle nucleation in the remote subtropical Pacific marine boundary layer, *J. Geophys. Res.*
1431 *Atmospheres*, 111, 2004JD005694, <https://doi.org/10.1029/2004JD005694>, 2006.

1432 Pirjola, L., O’Dowd, C. D., Brooks, I. M., and Kulmala, M.: Can new particle formation occur in the clean marine
1433 boundary layer?, *J. Geophys. Res. Atmospheres*, 105, 26531–26546, <https://doi.org/10.1029/2000JD900310>, 2000.

1434 Pope, S. B.: *Turbulent Flows*, 1st ed., Cambridge University Press, <https://doi.org/10.1017/CBO9780511840531>,
1435 2000.

- 1436 Pryor, S. C., Larsen, S. E., Sørensen, L. L., Barthelmie, R. J., Grönholm, T., Kulmala, M., Launiainen, S., Rannik, Ü.,
1437 and Vesala, T.: Particle fluxes over forests: Analyses of flux methods and functional dependencies, *J. Geophys. Res.*,
1438 112, D07205, <https://doi.org/10.1029/2006JD008066>, 2007.
- 1439 Quinn, P. K., Coffman, D. J., Johnson, J. E., Upchurch, L. M., and Bates, T. S.: Small fraction of marine cloud
1440 condensation nuclei made up of sea spray aerosol, *Nat. Geosci.*, 10, 674–679, <https://doi.org/10.1038/ngeo3003>, 2017.
- 1441 Rannik, Ü. and Vesala, T.: Autoregressive filtering versus linear detrending in estimation of fluxes by the eddy
1442 covariance method, *Bound.-Layer Meteorol.*, 91, 259–280, <https://doi.org/10.1023/A:1001840416858>, 1999.
- 1443 Sakai, R. K., Fitzjarrald, D. R., and Moore, K. E.: Importance of Low-Frequency Contributions to Eddy Fluxes
1444 Observed over Rough Surfaces, *J. Appl. Meteorol.*, 40, 2178–2192, [https://doi.org/10.1175/1520-0450\(2001\)040<2178:IOLFCT>2.0.CO;2](https://doi.org/10.1175/1520-0450(2001)040<2178:IOLFCT>2.0.CO;2), 2001.
- 1446 Sanchez, K. J., Zhang, B., Liu, H., Saliba, G., Chen, C.-L., Lewis, S. L., Russell, L. M., Shook, M. A., Crosbie, E. C.,
1447 Ziemba, L. D., Brown, M. D., Shingler, T. J., Robinson, C. E., Wiggins, E. B., Thornhill, K. L., Winstead, E. L.,
1448 Jordan, C., Quinn, P. K., Bates, T. S., Porter, J., Bell, T. G., Saltzman, E. S., Behrenfeld, M. J., and Moore, R. H.:
1449 Linking marine phytoplankton emissions, meteorological processes, and downwind particle properties with
1450 FLEXPART, *Atmospheric Chem. Phys.*, 21, 831–851, <https://doi.org/10.5194/acp-21-831-2021>, 2021.
- 1451 Schaller, C., Göckede, M., and Foken, T.: Flux calculation of short turbulent events – comparison of three methods,
1452 *Atmospheric Meas. Tech.*, 10, 869–880, <https://doi.org/10.5194/amt-10-869-2017>, 2017.
- 1453 Schmid, B., Tomlinson, J. M., Hubbe, J. M., Comstock, J. M., Mei, F., Chand, D., Pekour, M. S., Kluzek, C. D.,
1454 Andrews, E., Biraud, S. C., and McFarquhar, G. M.: The DOE ARM Aerial Facility, *Bull. Am. Meteorol. Soc.*, 95,
1455 723–742, <https://doi.org/10.1175/BAMS-D-13-00040.1>, 2014.
- 1456 Siebert, H., Szodry, K.-E., Egerer, U., Wehner, B., Henning, S., Chevalier, K., Lücknerath, J., Welz, O., Weinhold, K.,
1457 Laueremann, F., Gottschalk, M., Ehrlich, A., Wendisch, M., Fialho, P., Roberts, G., Allwayin, N., Schum, S., Shaw,
1458 R. A., Mazzoleni, C., Mazzoleni, L., Nowak, J. L., Malinowski, S. P., Karpinska, K., Kumala, W., Czyzewska, D.,
1459 Luke, E. P., Kollias, P., Wood, R., and Mellado, J. P.: Observations of Aerosol, Cloud, Turbulence, and Radiation
1460 Properties at the Top of the Marine Boundary Layer over the Eastern North Atlantic Ocean: The ACORES Campaign,
1461 *Bull. Am. Meteorol. Soc.*, 102, E123–E147, <https://doi.org/10.1175/BAMS-D-19-0191.1>, 2021.
- 1462 Spirig, C., Neftel, A., Ammann, C., Dommien, J., Grabmer, W., Thielmann, A., Schaub, A., Beauchamp, J., Wisthaler,
1463 A., and Hansel, A.: Eddy covariance flux measurements of biogenic VOCs during ECHO 2003 using proton transfer
1464 reaction mass spectrometry, *Atmospheric Chem. Phys.*, 5, 465–481, <https://doi.org/10.5194/acp-5-465-2005>, 2005.
- 1465 Stull, R. B. (Ed.): *An Introduction to Boundary Layer Meteorology*, Springer Netherlands, Dordrecht,
1466 <https://doi.org/10.1007/978-94-009-3027-8>, 1988.
- 1467 Sun, Y., Jia, L., Chen, Q., and Zheng, C.: Optimizing Window Length for Turbulent Heat Flux Calculations from
1468 Airborne Eddy Covariance Measurements under Near Neutral to Unstable Atmospheric Stability Conditions, *Remote
1469 Sens.*, 10, 670, <https://doi.org/10.3390/rs10050670>, 2018.
- 1470 Torrence, C. and Compo, G. P.: *A Practical Guide to Wavelet Analysis.*, *Bull. Am. Meteorol. Soc.*, 79, 61–78,
1471 [https://doi.org/10.1175/1520-0477\(1998\)079<0061:APGTWA>2.0.CO;2](https://doi.org/10.1175/1520-0477(1998)079<0061:APGTWA>2.0.CO;2), 1998.
- 1472 Wang, J., Pikridas, M., Spielman, S. R., and Pinterich, T.: A fast integrated mobility spectrometer for rapid
1473 measurement of sub-micrometer aerosol size distribution, Part I: Design and model evaluation, *J. Aerosol Sci.*, 108,
1474 44–55, <https://doi.org/10.1016/j.jaerosci.2017.02.012>, 2017a.
- 1475 Wang, J., Pikridas, M., Pinterich, T., Spielman, S. R., Tsang, T., McMahon, A., and Smith, S.: A Fast Integrated
1476 Mobility Spectrometer for rapid measurement of sub-micrometer aerosol size distribution, Part II: Experimental
1477 characterization, *J. Aerosol Sci.*, 113, 119–129, <https://doi.org/10.1016/j.jaerosci.2017.05.001>, 2017b.

1478 Wang, J., Wood, R., Jensen, M., Azevedo, E., Bretherton, C., and Chand, D.: Aerosol and Cloud Experiments in
1479 Eastern North Atlantic (ACE-ENA) Field Campaign Report, 2019.

1480 Weber, R. J., Marti, J. J., McMurry, P. H., Eisele, F. L., Tanner, D. J., and Jefferson, A.: Measurements of new particle
1481 formation and ultrafine particle growth rates at a clean continental site, *J. Geophys. Res. Atmospheres*, 102, 4375–
1482 4385, <https://doi.org/10.1029/96JD03656>, 1997.

1483 Weber, R. J., Clarke, A. D., Litchy, M., Li, J., Kok, G., Schillawski, R. D., and McMurry, P. H.: Spurious aerosol
1484 measurements when sampling from aircraft in the vicinity of clouds, *J. Geophys. Res. Atmospheres*, 103, 28337–
1485 28346, <https://doi.org/10.1029/98JD02086>, 1998.

1486 Wiedensohler, A., Covert, D. S., Swietlicki, Erik., Aalto, Pasi., Heintzenberg, Jost., and Leck, C.: Occurrence of an
1487 ultrafine particle mode less than 20 nm in diameter in the marine boundary layer during Arctic summer and autumn,
1488 *Tellus B*, 48, 213–222, <https://doi.org/10.1034/j.1600-0889.1996.t011-1-00006.x>, 1996.

1489 Wolfe, G. M., Kawa, S. R., Hanisco, T. F., Hannun, R. A., Newman, P. A., Swanson, A., Bailey, S., Barrick, J.,
1490 Thornhill, K. L., Diskin, G., DiGangi, J., Nowak, J. B., Sorenson, C., Bland, G., Yungel, J. K., and Swenson, C. A.:
1491 The NASA Carbon Airborne Flux Experiment (CARAFE): instrumentation and methodology, *Atmospheric Meas.*
1492 *Tech.*, 11, 1757–1776, <https://doi.org/10.5194/amt-11-1757-2018>, 2018.

1493 Wood, R. and Bretherton, C. S.: Boundary Layer Depth, Entrainment, and Decoupling in the Cloud-Capped
1494 Subtropical and Tropical Marine Boundary Layer, *J. Clim.*, 17, 3576–3588, [https://doi.org/10.1175/1520-0442\(2004\)017<3576:BLDEAD>2.0.CO;2](https://doi.org/10.1175/1520-0442(2004)017<3576:BLDEAD>2.0.CO;2), 2004.

1496 Wood, R., Wyant, M., Bretherton, C. S., Rémillard, J., Kollias, P., Fletcher, J., Stemmler, J., de Szoeko, S., Yuter, S.,
1497 Miller, M., Mechem, D., Tselioudis, G., Chiu, J. C., Mann, J. A. L., O’Connor, E. J., Hogan, R. J., Dong, X., Miller,
1498 M., Ghate, V., Jefferson, A., Min, Q., Minnis, P., Palikonda, R., Albrecht, B., Luke, E., Hannay, C., and Lin, Y.:
1499 Clouds, Aerosols, and Precipitation in the Marine Boundary Layer: An Arm Mobile Facility Deployment, *Bull. Am.*
1500 *Meteorol. Soc.*, 96, 419–440, <https://doi.org/10.1175/BAMS-D-13-00180.1>, 2015.

1501 Wulfmeyer, V., Muppa, S. K., Behrendt, A., Hammann, E., Späth, F., Sorbjan, Z., Turner, D. D., and Hardesty, R.
1502 M.: Determination of Convective Boundary Layer Entrainment Fluxes, Dissipation Rates, and the Molecular
1503 Destruction of Variances: Theoretical Description and a Strategy for Its Confirmation with a Novel Lidar System
1504 Synergy, *J. Atmospheric Sci.*, 73, 667–692, <https://doi.org/10.1175/JAS-D-14-0392.1>, 2016.

1505 Zhang, J., Chen, Y.-S., Yamaguchi, T., and Feingold, G.: Cloud water adjustments to aerosol perturbations are
1506 buffered by solar heating in non-precipitating marine stratocumuli, *Atmospheric Chem. Phys.*, 24, 10425–10440,
1507 <https://doi.org/10.5194/acp-24-10425-2024>, 2024.

1508 Zheng, G., Wang, Y., Aiken, A. C., Gallo, F., Jensen, M. P., Kollias, P., Kuang, C., Luke, E., Springston, S., Uin, J.,
1509 Wood, R., and Wang, J.: Marine boundary layer aerosol in the eastern North Atlantic: seasonal variations and key
1510 controlling processes, *Atmospheric Chem. Phys.*, 18, 17615–17635, <https://doi.org/10.5194/acp-18-17615-2018>,
1511 2018.

1512 Zheng, G., Wang, Y., Wood, R., Jensen, M. P., Kuang, C., McCoy, I. L., Matthews, A., Mei, F., Tomlinson, J. M.,
1513 Shilling, J. E., Zawadowicz, M. A., Crosbie, E., Moore, R., Ziemba, L., Andreae, M. O., and Wang, J.: New particle
1514 formation in the remote marine boundary layer, *Nat. Commun.*, 12, 527, <https://doi.org/10.1038/s41467-020-20773-1>, 2021.
1515

1516

▼
▲
Page 6: [1] Deleted Ajmal Rasheeda Satheesh 5/15/26 9:08:00 PM

▼
▲
Page 19: [2] Deleted Ajmal Rasheeda Satheesh 5/16/26 12:04:00 AM

▼
▲
Page 19: [3] Formatted Ajmal Rasheeda Satheesh 4/28/26 8:27:00 PM

Font color: Blue

▼
▲
Page 19: [3] Formatted Ajmal Rasheeda Satheesh 4/28/26 8:27:00 PM

Font color: Blue

▼
▲
Page 19: [4] Deleted Ajmal Rasheeda Satheesh 5/13/26 10:20:00 AM

▼
▲
Page 19: [4] Deleted Ajmal Rasheeda Satheesh 5/13/26 10:20:00 AM

▼
▲
Page 19: [4] Deleted Ajmal Rasheeda Satheesh 5/13/26 10:20:00 AM

▼
▲
Page 19: [4] Deleted Ajmal Rasheeda Satheesh 5/13/26 10:20:00 AM

▼
▲
Page 19: [4] Deleted Ajmal Rasheeda Satheesh 5/13/26 10:20:00 AM

▼
▲
Page 19: [5] Formatted Ajmal Rasheeda Satheesh 4/28/26 8:27:00 PM

Font color: Blue

▼
▲
Page 19: [5] Formatted Ajmal Rasheeda Satheesh 4/28/26 8:27:00 PM

Font color: Blue

▼
▲
Page 19: [5] Formatted Ajmal Rasheeda Satheesh 4/28/26 8:27:00 PM

Font color: Blue

▼
▲
Page 19: [5] Formatted Ajmal Rasheeda Satheesh 4/28/26 8:27:00 PM

Font color: Blue

▼
▲
Page 19: [5] Formatted Ajmal Rasheeda Satheesh 4/28/26 8:27:00 PM

Font color: Blue

▼
▲
Page 19: [5] Formatted Ajmal Rasheeda Satheesh 4/28/26 8:27:00 PM

Font color: Blue

▲

Page 19: [5] Formatted **Ajmal Rasheeda Satheesh** **4/28/26 8:27:00 PM**

Font color: Blue

Page 19: [5] Formatted **Ajmal Rasheeda Satheesh** **4/28/26 8:27:00 PM**

Font color: Blue

Page 19: [5] Formatted **Ajmal Rasheeda Satheesh** **4/28/26 8:27:00 PM**

Font color: Blue

Page 19: [5] Formatted **Ajmal Rasheeda Satheesh** **4/28/26 8:27:00 PM**

Font color: Blue

Page 19: [5] Formatted **Ajmal Rasheeda Satheesh** **4/28/26 8:27:00 PM**

Font color: Blue

Page 19: [5] Formatted **Ajmal Rasheeda Satheesh** **4/28/26 8:27:00 PM**

Font color: Blue

Page 19: [5] Formatted **Ajmal Rasheeda Satheesh** **4/28/26 8:27:00 PM**

Font color: Blue

Page 19: [5] Formatted **Ajmal Rasheeda Satheesh** **4/28/26 8:27:00 PM**

Font color: Blue

Page 19: [5] Formatted **Ajmal Rasheeda Satheesh** **4/28/26 8:27:00 PM**

Font color: Blue

Page 19: [5] Formatted **Ajmal Rasheeda Satheesh** **4/28/26 8:27:00 PM**

Font color: Blue

Page 19: [5] Formatted **Ajmal Rasheeda Satheesh** **4/28/26 8:27:00 PM**

Font color: Blue

Page 19: [5] Formatted **Ajmal Rasheeda Satheesh** **4/28/26 8:27:00 PM**

Font color: Blue

Page 19: [5] Formatted **Ajmal Rasheeda Satheesh** **4/28/26 8:27:00 PM**

Font color: Blue

Page 19: [5] Formatted **Ajmal Rasheeda Satheesh** **4/28/26 8:27:00 PM**

Font color: Blue

Page 19: [5] Formatted **Ajmal Rasheeda Satheesh** **4/28/26 8:27:00 PM**

Font color: Blue

▲
Page 19: [5] Formatted **Ajmal Rasheeda Satheesh** **4/28/26 8:27:00 PM**

Font color: Blue

▲
Page 19: [5] Formatted **Ajmal Rasheeda Satheesh** **4/28/26 8:27:00 PM**

Font color: Blue

▲
Page 19: [5] Formatted **Ajmal Rasheeda Satheesh** **4/28/26 8:27:00 PM**

Font color: Blue

▲
Page 19: [5] Formatted **Ajmal Rasheeda Satheesh** **4/28/26 8:27:00 PM**

Font color: Blue

▲
Page 19: [5] Formatted **Ajmal Rasheeda Satheesh** **4/28/26 8:27:00 PM**

Font color: Blue

▲
Page 19: [6] Deleted **Ajmal Rasheeda Satheesh** **4/27/26 7:21:00 PM**

✖